AMPA receptors at ribbon synapses in the mammalian retina: kinetic models and molecular identity

Espen Hartveit[1], Bas-Jan Zandt[1,2], Eirik Madsen[1,3], Áurea Castilho[1], Svein Harald Mørkve[1,4] and Margaret Lin Veruki[1]

[1] University of Bergen, Department of Biomedicine, Bergen, Norway.

[2] Current affiliation: Blue Brain Project, École polytechnique fédérale de Lausanne (EPFL), Geneva, Switzerland.

[3] Current affiliation: Førde Central Hospital, Department of Radiology, Førde, Norway.

[4] Current affiliation: Haukeland University Hospital, Department of Neurosurgery and Department of Radiology, Bergen, Norway.

Corresponding authors: Espen Hartveit and Margaret L. Veruki**,** University of Bergen, Department of Biomedicine, Jonas Lies vei 91**,** N-5009 Bergen**,** Norway. espen.hartveit@biomed.uib.no**;** margaret.veruki@biomed.uib.no

Number of pages: 68. **Number of figures:** 13. **Number of tables:** 4

Running title: Kinetic models and identity of AMPA receptors in AII amacrine cells

Key words: amacrine cells, glutamate receptors, kinetic scheme, patch clamp, retina

Acknowledgments This work was supported by The Research Council of Norway (NFR 161217, 178105, and 214216 to E.H., NFR 213776 to M.L.V.) and the Faculty of Medicine and Dentistry at the University of Bergen (fellowships for E.M. and S.H.M.). We thank Dr. Catherine W. Morgans for advice on antibodies and immunocytochemistry and Torhild Sunde for excellent technical assistance. The confocal imaging was performed at the Molecular Imaging Center (MIC) and was supported by the Department of Biomedicine and the Faculty of Medicine and Dentistry at the University of Bergen.

Abstract

In chemical synapses, neurotransmitter molecules released from presynaptic vesicles activate populations of postsynaptic receptors that vary in functional properties depending on their subunit composition. Differential expression and localization of specific receptor subunits are thought to play fundamental roles in signal processing, but our understanding of how that expression is adapted to the signal processing in individual synapses and microcircuits is limited. At ribbon synapses, glutamate release is independent of action potentials and characterized by a high and rapidly changing rate of release. Adequately translating such presynaptic signals into postsynaptic electrical signals poses a considerable challenge for the receptor channels in these synapses. Here, we investigated the functional properties of AMPA receptors of AII amacrine cells in rat retina that receive input at spatially segregated ribbon synapses from OFF-cone and rod bipolar cells. Using patch-clamp recording from outside-out patches, we measured the concentration dependence of response amplitude and steady-state desensitization, the single-channel conductance and the maximum open probability. The GluA4 subunit seems critical for the functional properties of AMPA receptors in AII amacrines and immunocytochemical labeling suggested that GluA4 is located at synapses made by both OFF-cone bipolar cells and rod bipolar cells. Finally, we used a series of experimental observables to develop kinetic models for AII amacrine AMPA receptors and subsequently used the models to explore the behavior of the receptors and responses generated by glutamate concentration profiles mimicking those occuring in synapses. These models will facilitate future *in silico* modeling of synaptic signaling and processing in AII amacrine cells.

Introduction

Neurotransmitter receptors play a fundamental role in the signal processing that takes place in different synapses, circuits and networks of the nervous system. Understanding how their differential expression and localization are adapted to and contribute to this processing is of fundamental importance (Silver et al., 2016). Neurotransmitter molecules released from synaptic vesicles can bind to and activate heterogeneous receptor populations, including ligand-gated ion channels, located in the membrane of the postsynaptic neuron. This heterogeneity is expressed both within a single postsynaptic density, at different synapses received by a single neuron, and at synapses made by the same neuron onto different postsynaptic targets (Shepherd and Grillner, 2010; Smart and Paoletti, 2012). The different types of receptor channels that recognize a given neurotransmitter typically differ in functional properties such as affinity for the neurotransmitter, single-channel conductance, kinetics, selectivity and permeability for specific ions, developmental regulation, and influence on downstream signaling pathways (Higley and Sabatini, 2012; Smart and Paoletti, 2012). There is strong evidence that the subunit composition of ligand-gated ion channels is of critical importance for the specific functional and signaling properties of a given receptor channel (Traynelis et al., 2010). However, despite strong evidence for differential expression of receptor subunits, little is known with respect to how this is adapted to or mediates the signal processing taking place in specific synapses, microcircuits and networks.

In the retina, synaptic release of glutamate from both photoreceptor and bipolar cells (Massey and Maguire, 1995; Thoreson and Witkovsky, 1999) is not triggered by presynaptic action potentials which are largely absent from these cells. Instead, synaptic transmission is characterized both by transient release and by continuous variation of an overall high release rate that can be maintained over longer periods of time (Heidelberger et al., 2005). Similar to sensory neurons in the auditory and vestibular systems, photoreceptor and bipolar cells have evolved specific structural components, known as synaptic ribbons, that seem to be of crucial importance for this specialized release (Lenzi and von Gersdorff, 2001; Lagnado and Schmitz, 2015). Whereas our understanding of synaptic release at ribbon synapses has made major advances in recent years, the complementary understanding of the postsynaptic mechanisms at ribbon synapses is far from complete. Specifically, the high and rapidly

changing rate of vesicle release poses a considerable challenge with respect to how the presynaptic signals can be processed by glutamate receptors and adequately translated into electrical signals in the postsynaptic neurons. To elucidate molecular events and signaling in these synapses will require computational modeling at the microphysiological level (e.g. Coggan et al., 2005), but developing realistic models requires detailed knowledge of molecular mechanisms, reaction kinetics and ultrastructural organization. The AII amacrine cell in the rod pathway of the mammalian retina is a particularly interesting case as it receives glutamatergic input at ribbon synapses made by both rod and OFF-cone bipolar cells to spatially distinct regions of the dendritic tree. Here, we investigated the functional properties of AMPA receptors of AII amacrine cells in rat retina and developed kinetic models that reproduce a range of experimental observations. In addition, we investigated the molecular basis for the distinct functional properties with immunocytochemical labeling of the AMPA receptor subunit GluA4, together with pre- and postsynaptic markers. Taken together, the functional properties and location of the GluA4 subunit suggests that it plays an important role in determining the functional properties of AMPA receptors expressed by AII amacrine cells and is involved in mediating synaptic input from both rod and OFF-cone bipolar cells.

Materials and methods

Retinal slice preparation and visual targeting of neurons

General aspects of the methods have previously been described in detail (Hartveit, 1996). Female albino rats (4 - 7 weeks postnatal) were deeply anaesthetized with halothane or isoflurane in oxygen and killed by cervical dislocation (procedure approved under the surveillance of the Norwegian Animal Research Authority). Retinal slices were visualized with a ×40 water immersion objective and infrared differential interference contrast (IR-DIC) videomicroscopy (Axioskop FS2; Zeiss). Patch pipettes were pulled from thick-walled borosilicate glass (outer diameter, 1.5 mm; inner diameter, 0.86 mm; BF150-86-10; Sutter Instrument). When filled with intracellular solution, the recording pipettes typically had resistances of 5 - 7 MΩ for recordings from both outside-out patches and nucleated patches. Outside-out patch recordings were established by slowly withdrawing the pipette after

establishing the whole-cell configuration. To establish nucleated patch recordings (Sather et al., 1992), we applied continuous light suction (~ -50 mbar) during the withdrawal. In both cases, successful isolation of a patch was indicated by a reduction in membrane capacitance, revealed as current transients of the opposite polarity of those electronically cancelled in the whole-cell configuration. Readjustment of the C_{slow} neutralization circuitry of the patch-clamp amplifier cancelled the capacitance transients. For most recordings, pipettes were coated with dental wax (to reduce capacitance) and fire-polished immediately before use. The reference electrode (Ag - AgCl wire) was immersed directly in the recording chamber or connected to the recording chamber via an electrolyte-agar or a solution bridge. Recordings were carried out at room temperature (22 - 25 °C).

Solutions and drugs

The extracellular perfusing solution was continuously bubbled with 95% O_2 - 5% CO_2 and had the following composition (in mM): 125 NaCl, 25 $NaHCO_3$, 2.5 KCl, 2.5 $CaCl_2$, 1 $MgCl_2$, 10 glucose (pH 7.4). For recordings from conventional and nucleated outside-out patches, the pipettes were filled with (in mM): 125 CsCl, 10 Hepes, 1 $CaCl_2$, 8 NaCl, 5 EGTA, 4 MgATP, 15 tetraethylammonium chloride (pH was adjusted to 7.3 with CsOH). Lucifer yellow was added at a concentration of 1 mg/ml to the intracellular solutions for visualization of cells at the end of the recordings. Theoretical liquid junction potentials were calculated with the computer program JPCalcW (Molecular Devices) and holding potentials were corrected for the liquid junction potentials on-line by the data acquisition software (see below).

Extracellular solutions with different concentrations of glutamate were prepared as follows. First, we made a stock solution with 100 mM glutamate by adding equimolar amounts of L-glutamic acid (Tocris Bioscience) and NaOH to a solution containing (in mM): 45 NaCl, 2.5 KCl, 2.5 $CaCl_2$, 1 $MgCl_2$, 5 hemiNa-Hepes, and 10 glucose (pH was adjusted to 7.4 with HCl). Different concentrations of glutamate, ranging from 2.5 μM to 30 mM, were obtained by diluting the 100 mM glutamate stock solution with a solution containing (in mM): 145 NaCl, 2.5 KCl, 2.5 $CaCl_2$, 1 $MgCl_2$, 5 hemiNa-Hepes, and 10 glucose (when necessary, pH was adjusted to 7.4 with HCl).

Ultrafast drug application

Ultrafast application of glutamate to outside-out patches (Jonas, 1995) was performed as previously described (e.g. Veruki et al., 2003). Glutamate pulses were applied with ≥ 4 s intervals from a theta-tube application pipette (nominal septum thickness ~117 μm; final tip diameter ~300 μm; Hilgenberg). The pipette tip with the outside-out patch was positioned ~100 μm away from the tip of the application pipette, close to the interface between control solution (without glutamate) and glutamate-containing solution continuously flowing out of each barrel. One barrel of the theta-tube application pipette was connected to a six-channel manifold that allowed switching between different test solutions, the other barrel was connected to the control solution. The control solution had the following composition (in mM): 145 NaCl, 2.5 KCl, 2.5 $CaCl_2$, 1 $MgCl_2$, 5 hemiNa-Hepes, and 10 glucose (pH adjusted to 7.4 with HCl). The solution flow rate (4 - 5 ml/h) was maintained by syringe pumps (KDS220; KD Scientific) controlled by the data acquisition software (see below). Concentration jumps of glutamate to the patch were performed by rapidly moving the position of the application pipette and thus the interface between the two solutions. The application pipette was mounted on a piezo actuator (LSS-3100/PZS-100HS; Burleigh Instruments Inc.) operated by an amplifier (PZ-150M; Burleigh Instruments Inc.) that received square-wave voltage pulses from the ITC-16 interface (see below). Before being fed to the amplifier, the voltage pulses were conditioned by an electronic circuit consisting of an RC-filter and an inductive element to avoid sharp voltage transients.

The solution exchange time was measured as the change in liquid junction current of an open-tip patch pipette upon a change from normal, Hepes-buffered extracellular solution to the same solution diluted to 10% with distilled water. Rise time was calculated as the interval between 20% and 80% of the peak amplitude relative to baseline and, under optimal conditions, ranged between 100 - 400 μs. The optimal position of the patch pipette in relation to the application pipette was mapped out at the start of each experiment. For some recordings, the patch was blown away at the end of the recording and the solution exchange time was verified by switching to the 10% dilute solution.

For nucleated patch recordings, the same equipment and procedures as described above were used. However, because of the larger size of nucleated patches, the solution

exchange times were slower than predicted from the measurements of open-tip patch pipette responses in these recordings. Nucleated patch recordings were used to measure steady-state (plateau) responses during longer-lasting applications of glutamate.

Data acquisition. Voltage-clamp recordings were made with an EPC9-dual amplifier (HEKA Elektronik) controlled by Pulse or Patchmaster software (HEKA Elektronik). Cells and patches were held at a potential of -60 mV. Application of voltage stimuli and digital sampling of the analog signals were performed via an ITC-16 interface built into the EPC9 amplifier. Before sampling, the signal was low-pass filtered (analog 3- and 4-pole Bessel filters in series) with a corner frequency (–3 dB) typically set to 2 kHz (in general between 1/12.5 and 1/3 of the inverse of the sampling interval; 10 - 100 μs). Capacitative currents caused by the recording pipette capacitance (C_{fast} function of the PatchMaster software) and the cell membrane capacitance (C_{slow} function of the PatchMaster software) were measured with the automatic capacitance neutralization network feature of the EPC9-dual.

General data analysis

Electrophysiological data were analyzed with FitMaster (HEKA Elektronik), IGOR Pro (WaveMetrics), AxoGraph X (AxoGraph Scientific), Excel (Microsoft) and GraphPad Prism (GraphPad Software). If required, recorded current signals were low-pass filtered at 2 kHz before analysis (-3 dB; digital non-lagging Gaussian filter).

The decay time-course of responses evoked by ultrafast application of agonist was estimated by curve fitting with exponential functions. For single exponential functions, we used the function:

$$I(t) = A\exp(-t/\tau) + I_{ss} \quad (1)$$

where *I(t)* is the current as a function of time, A is the amplitude at time 0, τ is the time constant, and I_{ss} is the steady-state current amplitude. For double exponential functions, we used the function:

$$I(t) = A_1\exp(-t/\tau_1) + A_2\exp(-t/\tau_2) + I_{ss} \quad (2)$$

where *I(t)* is the current as a function of time, A_1 and A_2 are the amplitudes at time 0 of the first and second exponential components, τ_1 and τ_2 are the time constants of the first and

second exponential components, and I_{ss} is the steady-state current amplitude. Fitting was started 50 - 700 μs after the peak amplitude. For double exponential functions, the amplitude contribution for A_x (A_1 or A_2) was calculated as $100\% \times (A_x/(A_1+A_2))$. The relative amplitude of fitted exponentials depends on the definition of time 0, which we defined as the start of the response, determined by eye as the point in time at which the current rose from the baseline noise.

The amplitude of glutamate-evoked current responses was calculated as either the peak or the mean current between vertical cursors positioned on the current traces. For each patch, the response at each concentration of glutamate was typically calculated from the average of 5 - 25 repetitions. Concentration-response data were normalized to the response at a fixed concentration and fitted with a Hill-type equation of the following form:

$$I = \frac{I_{max}}{1+10^{(\log_{10}(EC_{50})-\log_{10}[A])n_H}} \quad (3)$$

where I is the current at a given concentration of agonist ([A]), I_{max} is the maximum current, EC_{50} is the agonist concentration giving rise to half-maximal current, and n_H is the Hill coefficient. As the best-fit parameters were subsequently used for kinetic model fitting, it is important to realize that the Hill equation is an empirical description which cannot be derived from any realistic physical mechanism and the parameters EC_{50} and n_H have no direct physical significance. Importantly, there is no reason to suppose that n_H will be an integer and it cannot be interpreted as the number of molecules that combine with a receptor (e.g. Wyman and Gill, 1990). To obtain symmetric confidence intervals, the $\log_{10}(EC_{50})$ was used as the variable for fitting rather than the EC_{50} (see "Confidence intervals of the EC_{50}", GraphPad Software, http://www.graphpad.com/guides/prism/6/curve-fitting/index.htm?reg_why_prism_fits_the_logec50_rat.htm). For experiments with steady-state desensitization following pre-exposure to agonist, the agonist-evoked response to application of a fixed concentration of agonist was normalized to the response obtained without pre-exposure to agonist. Data points were plotted as agonist-evoked response vs. $\log_{10}$ of the concentration of agonist during pre-incubation. Concentration-inhibition curves were generated by fitting with an equation equivalent to Eq. 3 giving values for $\log_{10}(IC_{50})$

($\log_{10}$ of the pre-incubation agonist concentration giving rise to half-maximal inhibition) and n_H. Curve fitting of concentration-response and concentration-inhibition data (GraphPad Prism) took into account the number of patches and the response amplitude scatter among the replicates for each concentration of glutamate (see Colquhoun et al., 1992, for a similar approach).

Data are presented as means ± SEM (or SE where appropriate) and percentages are presented as percentage of control. Statistical analyses were performed using Student's two-tailed *t* tests (unpaired, unless otherwise stated) and differences were considered significant at the $P < 0.05$ level. The bias of a parameter estimate (a') relative to the nominal (true) parameter value (a) was calculated as: $100\% \times (a' - a)/a$. For illustration purposes, most raw data-records were either low-pass filtered (-3 dB; digital non-lagging Gaussian filter at 0.5 - 2 kHz) or smoothed by a binomial smoothing function (IGOR Pro) to emphasize the kinetics of the response. Unless otherwise noted, the current traces shown in the figures represent individual traces.

Non-stationary noise analysis

We applied non-stationary noise analysis to responses obtained by ultrafast application of brief (~1 ms) pulses of glutamate (3 mM) to outside-out patches in order to estimate the apparent single-channel conductance and open probability of the glutamate receptors (for details, see Hartveit and Veruki, 2007). The ensemble mean for a series of consecutive responses without run-down was binned into 20 segments along the ordinate, with each bin corresponding on average to an equal number of channel closings during the decay phase. Data points for ensemble variance *versus* mean current for the decay phase were fitted with the following function:

$$\sigma^2(I) = iI - I^2/N + \sigma_b^2 \quad (4)$$

where i is the apparent single-channel current, I is the mean current, N is the number of available channels in the patch and σ_b^2 is the background variance. The open probability of the receptor channels in the patch is determined at any given point in time by:

$$P_{open} = I/iN \quad (5)$$

where P_{open} is the open probability of the receptor channels, i is the apparent single-channel current, I is the mean current and N is the number of available channels. The single-channel chord conductance was calculated as:

$$\gamma = i/(V_m - E_{rev}) \quad (6)$$

where i is the apparent single-channel current, V_m is the holding potential (-60 mV) and E_{rev} is the reversal potential (set to 0 mV; Mørkve et al., 2002; Veruki et al., 2003).

Kinetic model fitting and simulations

Macroscopic (deterministic) simulations of ion channel current responses were based on two different experimentally derived Markov-type kinetic models. One model was originally developed for glutamate receptors expressed by cerebellar Purkinje cells (Häusser and Roth, 1997) and the other model was originally developed for specific AMPA receptors heterologously expressed in HEK 293 cells (Robert and Howe, 2003). Macroscopic simulations were programmed in Matlab (MathWorks) and IGOR Pro, with the Matlab code used for fitting models to our experimental data. We calculated state occupancies by numerical integration of a set of coupled first-order ordinary differential equations. Since the system of equations is stiff, i.e. it contains time constants that differ by several orders of magnitude, the equations were solved using Matlab's *ode15s* (a solver for stiff differential equations using a variable time step). The algorithm was set to return the output at time points with a fixed interval of 0.1 ms. The absolute and relative tolerances were set to 10^{-4} and we checked that further decreasing these values did not significantly change the calculated model output (less than 0.1% change was observed when the tolerances were reduced by a factor of 10).

The agonist waveform was modeled as the product of two error functions to mimic the finite rise and decay times in physiological experiments:

$$[A](t) = f \times [A]_{peak} \times \left(1 + erf\left(a(t-b)\right)\right) \times \left(1 + erf\left(-a\left(t-(b+c)\right)\right)\right) \quad (7)$$

where $[A](t)$ is the agonist concentration profile as a function of time, f is a scaling factor (set to 0.25), $[A]_{peak}$ is the peak concentration of agonist, *erf* is the error function, a determines the steepness of the rise and decay phases (set to 4.8 ms^{-1} to generate a 20-80% rise time of 0.25

ms), t is time, b is the delay to onset of the pulse, and c is the pulse duration (full width at half maximum). The resulting traces of the open probability were low-pass filtered at 2 kHz (-3 dB cut-off) by convolving them with a Gaussian function:

$$A \times e^{(-t/w)^2} \tag{8}$$

(with w = 93.7 μs) before analysis to match the analysis of experimental data. The simulation results were analyzed using built-in functions of Matlab, including non-linear curve fitting, with the goal of matching the procedures used to analyze the experimental data.

The goal of the model optimization was to find a set of rate constants for each of the two kinetic models that would minimize the difference between the model output and the experimental results (target) for a given set of observables obtained in the present and a previous study from our laboratory (Veruki et al., 2003). During model optimization, the observables and their deviation from the target observables were calculated for a given set of parameters. The model optimization minimized an objective function E, defined as the sum-of-squares of the deviations of the model output X_{mod} from the experimental target observables X_{exp} (see Results), normalized by the corresponding experimental standard error (SE):

$$E = \sum_X \left(\frac{X_{mod} - X_{\exp}}{SE_X} \right)^2 \tag{9}$$

To aid in interpreting the goodness of a particular fit, we also calculated the square root of the mean of the squares of the normalized deviations (root-mean-square; RMS):

$$RMS = \sqrt{\frac{1}{N} \sum_X \left(\frac{X_{mod} - X_{\exp}}{SE_X} \right)^2} \tag{10}$$

where N is the number of observables. In addition, to prevent the algorithm from selecting very different rate constants for the binding (or unbinding) of glutamate by receptors in the non-desensitized and desensitized states, the ratios of these rate constants (see Results for each kinetic model) were softly constrained such that a ratio of 1:10 in the rate constants would be penalized as much as an error of 1 SE. This was accomplished by adding the $\log_{10}$ of these ratios to the observables, with a target value of 0 and a weight value of 1. With this constraint, the fitting routine preferred slightly larger errors in the observables over very

disparate rate constants and in practice constrained the relevant ratios to a maximum of approximately 1:10.

For the model optimization, we used the *MultiStart* algorithm in Matlab to obtain the location and objective function value of local minima in the search space. Multiple local minima are found by performing local optimization from multiple starting points. Starting points were randomly selected from an even distribution of points in a bound region of parameter space. The *MultiStart* algorithm was executed in parallel on 12 processor cores.

For the local optimization, we let *MultiStart* use the Levenberg-Marquardt algorithm (Marquardt, 1963) implemented in Matlab's *lsqnonlin* function (function tolerance set to 10^{-4}, position tolerance set to 10^{-5}, and minimum step for approximation of the Jacobian set to 10^{-4}). This algorithm uses the information of all individual deviations rather than the sum-of-squares alone, and typically converges after 5 - 10 iterations.

Bounds on the region from which starting points were sampled were selected after initial manual fitting and exploration of the parameter space. The center of the search space was set at a point around which reasonable fits were obtained and low and high search bounds were set by multiplying these rate constants by 0.5 and 2, respectively. These bounds did not constrain the local optimization. Maintenance of microscopic reversibility (Hille, 2001) differed between the two models which we used for fitting (see Results). To ensure proper scaling of the optimization problem, the search space was log-transformed, i.e. the algorithm searched in the space of $\{x_{01}, x_{12}, ...\} = \{\log_{10}(k_{01}), \log_{10}(k_{12}), ...\}$, where k_{ab} is the rate constant for the transition from state A to state B. For each optimization we typically let the algorithm run for a day, resulting in at least 300 local optimizations from which the local minimum with the smallest sum-of-squares deviation was selected. In practice, this was sufficient to obtain an optimal fit, as the objective function did not improve more than 10% after the first ~30 local optimizations. The best fit, i.e., the local minimum with the smallest sum-of-squares deviation was selected as the optimal model.

Stochastic simulations

For non-stationary and covariance analysis of simulated ion channel responses, we used stochastic (Monte Carlo or microscopic) simulations with AxoGraph X. The number of

receptor channels (N) was set to 50; the driving force (membrane potential minus reversal potential; V_m - E_{rev}) to -60 mV; the time interval to 10 μs; and for each condition an ensemble of events was generated by repeating the simulations 1000 times (n). To mimic one source of quantal variability, some simulations were run by varying the number of available receptor channels randomly between trials (N_{mean} = 50; Gaussian distribution with SD = 10). The single-channel conductance was specified for each model.

Bootstrap analysis

For simulated events, we estimated statistical errors in the best-fit parameters by bootstrap analysis (Efron and Tibshirani, 1993). We performed balanced resampling by generating 100 random lists of 1000 event numbers (from 1 to 1000) with custom routines in IGOR Pro. Each number corresponded to an event in the original ensemble of simulated events, and each list of numbers was subsequently used to generate a new (synthetic) data set with 1000 events.

Autocovariance analysis

Autocovariance (for simplicity, henceforth referred to as covariance) functions were calculated from an n-by-m event matrix (n events and m sample points for each event) in IGOR Pro (see Hartveit and Veruki, 2006). The resulting m-by-m covariance matrix is a measure of the linear strength between the m variables and can be stated as,

$$C_n(t_1,t_2) = \frac{1}{n-1}\sum_{i=1}^{n}\left[y_i(t_1)-\mu(t_1)\right]\left[y_i(t_2)-\mu(t_2)\right] \qquad (11)$$

where the y_i are the current values from the ith event and the μ are the means of the ny_i values. Each value in the covariance matrix, σ^2_{ij}, corresponds to the covariance between the corresponding columns i and j in the original event matrix. The diagonal of the covariance matrix (i=j) corresponds to the variance values for the n columns of the event matrix. For a given center point (t_c), the decay of a covariance function, $C(t_1, t_2)$, can be estimated by fitting with exponential functions such that each decay time constant corresponds to a correlation time (termed t_{corr}).

Calculating an apparent maximum P_{open} ($P_{open,\,max}$) for a kinetic scheme with multiple open states

From the experimental data, $P_{open,\,max}$ was determined by non-stationary noise analysis (see above). This analysis assumes a single open state (or multiple open states with the same conductance) and will not give the correct P_{open} for a channel with multiple conductance levels. We can, however, calculate an apparent $P_{open,\,max}$ for a receptor channel model with multiple conductance levels, i.e. the $P_{open,\,max}$ that would be obtained if the analysis procedure were applied to experimental data. Although there is no clear physiological interpretation of the apparent $P_{open,\,max}$, it can be used to correctly fit the model to the experimental observations.

To determine the apparent $P_{open,\,max}$, we calculated the average current and its variance predicted by the state occupancies in the model from a single simulation run of the model. The simulation provides a probability distribution, at each point in time, for a receptor channel to be in a certain state and to conduct a certain current. The average and variance for a single-channel current (I_1) are given by the mean and second moment around the mean, respectively, of the probability distribution:

$$\langle I_1 \rangle = \sum_n P_n i_n \tag{12}$$

$$\sigma^2(I_1) = \sum_n P_n (i_n - \langle I_1 \rangle)^2 \tag{13}$$

where $\langle . \rangle$ denotes the expectation value (average), $\sigma^2(.)$ denotes the variance, P_n denotes the probability of the channel to be in state n and i_n denotes the current conducted by state n. For N identical channels, these are multiplied by N:

$$\langle I \rangle = N \sum_n P_n i_n \tag{14}$$

$$\sigma^2(I) = N \sum_n P_n (i_n - \langle I_1 \rangle)^2 \tag{15}$$

Any states that have the same conductance can be treated as a single state, with identical conductance and a summed probability of the receptor channel being in that state, without affecting the value for current and its variance. Thus, for a receptor for which all open states conduct a current i_0 and all closed states conduct zero current, the equations reduce to their familiar form as used in non-stationary noise analysis:

$$\langle I \rangle = N\left(P_{open} i_0 + P_{closed} \times 0\right) = N\, P_{open}\, i_0 \tag{16}$$

$$\sigma^2(I) = N\, \left(P_{open}\left(i_0 - P_{open}\, i_0\right)^2 + P_{closed}\left(0 - P_{open} i_0\right)^2\right) \tag{17}$$

$$= i_0\langle I\rangle - \langle I\rangle^2/N \quad (18)$$

where P_{open} and P_{closed} are the sum of probabilities for each of the open and closed states, respectively, and $P_{\text{closed}} = P_{\text{open}} - 1$. Note that for experimental data, a constant σ_b^2 representing baseline noise is added to the variance (Eq. 4).

To determine $P_{\text{open, max}}$ for the model, we simulated the response evoked by a brief agonist pulse and calculated I and $\sigma^2(I)$ for all points in time according to Eq. 14 and Eq. 15 with $N = 1$. Then, the apparent $P_{\text{open, max}}$ was calculated by a procedure similar to that used for analysis of the experimental data. The peak current (I_{peak}) was found and data points of I and $\sigma^2(I)$ following I_{peak} were selected. $\sigma^2(I)$ was plotted against I and re-sampled at 100 evenly spaced points (in I) to avoid overweighting the current values in the tail of the response. A quadratic function, equivalent to Eq. 4, was fitted to the data points, giving values for the apparent N (N_{ap}) and i_0 ($i_{0,\text{ap}}$):

$$y = i_{0,ap}I - I^2/N_{ap} + \sigma_b \quad (19)$$

Finally, $P_{\text{open, max}}$ was calculated as:

$$P_{open,\ max} = I_{peak}/\left(i_{0,ap}N_{ap}\right) \quad (20)$$

We verified that when all open states were set to the same conductance, corresponding to the current i_0, this method resulted in the correct value for i_0, calculated $N_{\text{ap}} = 1$, and yielded a value for $P_{\text{open, max}}$ that was equal to the sum of the occupancies of the open states. For a model with different conductances for the open states, $i_{0,\text{ap}}$ will be between the currents of the different open states, whereas N_{ap} will deviate from 1 and will have no clear interpretation (cf. Hartveit and Veruki, 2006).

Cell injection and immunocytochemical labeling

For injecting AII amacrine cells with fluorescent dye, retinal slices were prepared as described earlier for electrophysiological recording. The live slices were visualized with a ×60 water immersion objective and Dodt gradient contrast on an Olympus BX51 WI microscope. Using a simultaneous combination of transmitted light and epifluorescence optics (filter set 49011 with the emission filter replaced with the long-pass filter ET510lp; Chroma), visually targeted AII amacrine cells were impaled with sharp microelectrodes with the tip filled with 5 mM Alexa Fluor 488 (Invitrogen / Thermo Fisher Scientific) dissolved in

200 mM KCl and backfilled with 200 mM KCl without dye. Microelectrodes were pulled from thin-walled borosilicate glass (outer diameter, 1.0 mm; inner diameter, 0.78 mm; BF100-78-10; Sutter Instrument). When filled with dye solution, injection pipettes typically had resistances of 125 - 175 MΩ. For injection, the microelectrode was connected to an intracellular amplifier (SEC-05LX; npi electronic) in bridge mode. For pipettes with resistances in the lower range, we sometimes applied a retaining current of +100 to +200 pA to reduce leakage of dye. After successful impalement, cells were injected with a current of -500 pA for 3-5 min (1 Hz; 900 ms on / 100 ms off). After injection, slices were fixed at room temperature for 10 - 15 min in 4% paraformaldehyde in 0.1 M phosphate buffer (PB; 0.081 M Na_2HPO_4 / 0.019 M NaH_2PO_4, pH = 7.4). Following fixation, slices were washed three times (5 min each) in 0.01 M phosphate-buffered saline (PBS; 0.01 M PB with 8.76 g NaCl and 0.2 g KCl per liter, pH = 7.4). Next, slices were incubated for 1 h at room temperature in antibody incubation solution (AIS) consisting of PBS with 5% normal goat serum (NGS; Sigma-Aldrich), 0.5% Triton X-100 (Sigma-Aldrich) and 1% NaN_3. Slices were then incubated overnight (at 4 °C) with primary antibody in AIS (for a summary of the primary antibodies used in the present study, see Table 1). The next day, slices were washed three times (10 min each) in PBS and incubated at room temperature with secondary antibody in AIS for 2 - 3 h. Secondary antibodies included goat anti-mouse and goat anti-rabbit coupled to Alexa 555 or Alexa 647 (Invitrogen / Thermo Fisher Scientific) used at a dilution of 1:500. Subsequently, the slices were washed three times (15 min each) in PBS and mounted in Vectashield (refractive index 1.450; Vector Laboratories) between two precision coverslips (0.17 mm thickness, tolerance ± 0.01 mm; Karl Hecht Assistent) separated by a 0.12 mm thick spacer disk (Electron Microscopy Sciences).

Table 1 near here

Confocal microscopy and image acquisition

Cell-injected and immunolabeled retinal slices were imaged on a TCS SP5 confocal microscope (Leica) equipped with a ×63 oil immersion objective (HCX PL APO CS UV, 1.4 NA; Leica). For fluorescence imaging, we used the following lasers and laser lines: Argon 488 nm (for Alexa Fluor 488 in the first channel), DPSS 561 nm (for Alexa Fluor 555 in the

second channel) and HeNe 633 nm (for Alexa Fluor 647 in the third channel). The emission bandwidths for the three channels were set to 498-530 nm, 570-595 nm and 650-700 nm, respectively. For each acquisition channel, offset and gain of the corresponding photomultiplier tube were adjusted to maximize the dynamic range, with minimal saturation at the highest intensities. An image stack was acquired as a series of optical slices (each slice 1024 × 1024 or 2048 × 2048 pixels, depending on the size and orientation of the injected cell) by sequential scanning (between frames) of the three different channels for each slice. For each of the three frames (corresponding to the three channels), each line was scanned two times and averaged to increase the signal-to-noise ratio (SNR). The confocal pin hole was set to one Airy unit (calculated for 580 nm light). To obtain well-sampled image stacks that could be processed with deconvolution (see "Image processing, deconvolution and analysis"), images were sampled at a rate close to the ideal Nyquist rate. The Nyquist sampling distance in the lateral direction was calculated as:

$$\Delta_x = \Delta_y = \frac{\lambda_{eff}}{4n \times \sin\alpha} \tag{21}$$

and for the axial direction, the Nyquist sampling distance was calculated as:

$$\Delta_z = \frac{\lambda_{eff}}{2n \times (1-\cos\alpha)} \tag{22}$$

where $\lambda_{eff} = 1/\left(\frac{1}{\lambda_{ex}} + \frac{1}{\lambda_{em}}\right)$, λ_{ex} is the wavelength of the excitation light, λ_{em} is the wavelength of the emission light, n is the lens medium refractive index (1.518 for the immersion oil), and α is the half-aperture angle of the the objective (reviewed by Heintzmann, 2006; see also https://svi.nl/NyquistRate). Depending on the digital zoom and the number of pixels in each image slice, the XY pixel size was either ~40 or ~43 nm. The focal plane interval was ~126 nm. All values were sufficient to satisfy Nyquist rate sampling according to the stated equations. All image stacks were acquired at 12 bit resolution and acquisition was controlled by LAS X software (Leica).

For one slice, we had access to a TCS SP8 confocal microscope (Leica) equipped with HyD detectors and a ×63 glycerol immersion objective (HC PL APO CS2 glycerol, 1.3 NA; Leica). Imaging was performed as described above, except that the confocal pinhole was set

to 0.5 Airy unit, the XY pixel size was set to ~45 nm, and the focal plane interval was set to ~150 nm, satisfying Nyquist rate sampling.

Image processing, deconvolution and analysis

Huygens Essential (version 14 - 16, 64 bit, Scientific Volume Imaging) was used to digitally deconvolve each channel in the image stack to remove noise (effectively increasing the SNR) and decrease axial and lateral blurring. The software reassigned out-of-focus light with a theoretically calculated point spread function, using the classic maximum likelihood estimation (CMLE) deconvolution algorithm. For each image stack, we estimated an optimal value for the user-selectable SNR parameter by repeating the deconvolution for several values of the SNR while keeping all other parameters and settings constant (see Zandt et al., 2017). In addition to reducing noise and decreasing blurring, deconvolution with Huygens Essential also (partially) compensates for spherical aberration that is aggravated by refractive index mismatch (between the lens immersion medium and the specimen embedding medium). In our case, the refractive index mismatch can be considered moderate and we observed moderate, but distinctly noticable spherical aberration at imaging depths of approximately ≥10 μm into the retina slices.

After deconvolution, we used the Object Analyzer module in Huygens Essential to analyze the spatial relationships between fluorescent structures corresponding to the (dye-filled) AII amacrine cell and immunolabeled punctae. To segment the structures of interest, we applied simple (global) thresholding. For optimal adjustment of the threshold intensity separately for each channel, we exported the deconvolved image stacks (in 16 bit TIFF format) to Amira (version 6, FEI / Thermo Fisher Scientific). As a first step, we selected the threshold automatically estimated according to Otsu's criterion (Otsu, 1979), using the "Auto Thresholding" function of Amira and increased or decreased this as was found necessary during visual inspection of the segmentation results using the "Edit Label Field" function and "Segmentation Editor" of Amira. When satisfactory threshold values were selected for each channel in the image stack, they were used for segmentation and subsequent object analysis in Huygens Essential. For segmentation of fluorescence signals corresponding to synaptic punctae, we also applied watershed segmentation (as implemented in Huygens Essential) to

separate merged objects arising from discrete overlapping punctae. We also applied the "sigma setting" to avoid over-segmentation by smoothing the image intensities with a Gaussian filter (σ = 1.0 μm). Following segmentation, objects smaller than 50 voxels were regarded as noise and were removed before analysis.

For segmented immunolabeled GluA4 punctae, we first used the Object Analyzer in Huygens to isolate all punctae that overlapped (intersected) spatially with an object belonging to the segmented AII amacrine cell. Overlap (intersection) means that two objects share one or more voxels within the segmented volumes. For the population of segmented and overlapping punctae the Object Analyzer then calculated a series of parameters, including center of mass (after intensity weighing of voxels), distance from the center of mass to the surface of the segmented AII amacrine, and the relative colocalization (measured as the fraction of the volume of a segmented punctum object, based on the number of voxels, that intersected with an object belonging to the segmented AII amacrine cell). To estimate the average signal around segmented objects corresponding to immunolabeled punctae in the same or the other channel(s) of an image stack, we used custom-written routines in IGOR Pro. For each 3D coordinate (corresponding to the center of mass of a specific immunolabeled punctum in the isolated population of punctae overlapping with the AII amacrine), a volume (corresponding to a square prism) centered around the coordinate was extracted from the image stack and combined with all the other extracted volumes to calculate the average across all 3D coordinates (for a given channel). The extracted volumes measured either 3 μm along the X and Y axes and 4 μm along the Z axis or 6 μm along the X and Y axes and 8 μm along the Z axis. We preferred the approach described here for object-based analysis of colocalization over alternative methods that involve rotating one imaging channel relative to the other(s) for several reasons. First, for image stacks acquired from vertical retinal slices, the anisotropy of the tissue means that rotation around the X or Z axis will reposition neuronal processes to locations where they do not belong (e.g. arboreal dendrites could end up in the outer plexiform layer). For rotation around the Y axis (along the major vertical axis of the cell), even minor asymmetries in branching could mean that processes would be relocated above the surface of the retinal slice. Second, when the density of punctae is high, there could easily be spatial overlap between segmented punctae and

neuronal processes for several alternative positions after rotation (for discussion, see Hoon et al., 2013).

Results

Identification of AII amacrine cells in retinal slices

AII amacrine cells in retinal slices were visually targeted for recording according to the following criteria: (1) location of the cell body at and across the border between the inner nuclear layer and the inner plexiform layer; (2) medium size of the cell body; and (3) a thick primary dendrite that tapers as it descends into the inner plexiform layer (Fig. 1a). Immediately after breaking into a cell and establishing the whole-cell recording configuration, the characteristic unclamped action currents (Mørkve et al., 2002), occurring both spontaneously and when evoked by 5 mV depolarizing voltage steps (Fig. 1b), confirmed the identity of the cell as an AII amacrine cell. In every case, when a cell was targeted according to the criteria indicated above and also displayed the characteristic unclamped action currents, fluorescence microscopy after the recording allowed morphological identification based on the presence of lobular appendages in sublamina *a* and arboreal dendrites in sublamina *b* of the inner plexiform layer.

Figure 1 near here

Concentration-response properties of glutamate receptors: peak responses

In the first set of experiments, the concentration-response properties were studied by ultrafast application of long pulses (100 ms) of glutamate (50 μM - 30 mM) to conventional outside-out patches. The responses evoked in a patch by application of four different concentrations of glutamate are illustrated in Fig. 1c. At these concentrations, glutamate pulses evoked responses that rose rapidly to a peak followed by a slower decay, corresponding to desensitization. At a glutamate concentration of 500 μM, the 20-80% rise time was ~785 μs and at 10 mM (the highest concentration tested for this patch), the rise time was ~378 μs (Fig. 1e). At lower concentrations of glutamate (≤50 μM), the response is expected to rise more slowly to a plateau (e.g. Häusser and Roth, 1997), without response reduction during the period of application. However, because of low channel density in most

patches, we often did not observe responses to the lowest concentrations tested (50 - 100 μM) which precluded further analysis at these concentrations. Importantly, the responses evoked by glutamate applied to outside-out patches from AII amacrine cells are mediated by AMPA receptors, as these cells do not express kainate receptors (Mørkve et al., 2002) and NMDA receptors expressed by AII amacrines (Hartveit and Veruki, 1997) are virtually absent from the cell body (Zhou et al., 2016).

All patches included in the analysis were tested with a reference concentration of 5 mM glutamate in addition to one or more other concentrations of glutamate. Only patches that displayed a peak response to 5 mM glutamate of ≥4 pA were included in the analysis. To construct concentration-response curves, the peak amplitude of the response at each concentration was normalized to the response at 5 mM. To correct for rundown during the period between application of the reference (5 mM) and test concentrations of glutamate, application of the test concentration was followed by another application of the reference concentration. For each patch, the peak current evoked by each test concentration was normalized to the expected response (evoked by 5 mM glutamate) at the same point in time, obtained by a linear curve fit to the data points obtained from 5 mM glutamate pulses before and after the test pulses. For each concentration of glutamate, we averaged the normalized responses of 4 - 16 patches. The data points were fitted with Eq. 3, yielding values for EC_{50} of 1.53 mM and n_H of 0.987 (Fig. 1e; n = 16 patches).

In a second series of experiments, the concentration-response properties were studied by ultrafast application of short pulses (nominal duration ~1.2 ms) of glutamate (50 μM - 30 mM) to conventional outside-out patches (Fig. 1f). For higher concentrations of glutamate, the peak responses evoked by short and long pulses should be identical (cf. Veruki et al., 2003), but for lower concentrations of glutamate, it could be expected that the maximum obtainable response would not be reached during the duration of the pulse. Nevertheless, when the data were analyzed in the same way as described for long pulses, we obtained similar values for EC_{50} (1.76 mM) and n_H (0.998; n = 1 - 7 patches for each data point; Fig. 1g).

Concentration-response properties of glutamate receptors: steady-state responses

For conventional outside-out patches, the strong desensitization observed for AMPA receptors of AII amacrine cells (Mørkve et al., 2002; Veruki et al., 2003) generated steady-state current responses that were too small to be adequately analyzed. Accordingly, to examine concentration-response properties for steady-state responses, we recorded instead from nucleated patches that contain a larger number of receptors. For nucleated patches, it is not possible to obtain ultrafast solution exchange with the technique used here, but for measurement of the steady-state response such rapid exchange is also not needed. Examples of glutamate-evoked responses from nucleated patches from AII amacrine cells were illustrated in a recent study from our laboratory (Castilho et al., 2015). We obtained responses to one or more test concentrations of glutamate (range 2.5 μM - 25 mM) from a total of 19 nucleated patches. All nucleated patches were also tested with a reference concentration of 1 mM glutamate and only those that displayed a steady-state response ≥ 1 pA to 1 mM glutamate were included in the analysis. For each nucleated patch, application of the various test concentrations was always preceded and followed by application of the reference concentration of glutamate (1 mM). Normalization of the response to each test concentration to the response to the reference concentration was performed as described above for experiments with conventional outside-out patches. For each concentration of glutamate, we averaged the (normalized) responses from 2 - 5 patches. The data points were fitted with Eq. 3, yielding values for EC_{50} of 693 μM and n_H of 0.554 (Fig. 1h; n = 19 patches). A lower EC_{50} for the steady-state response than for the peak response is a common observation for AMPA receptors (e.g. Robert and Howe, 2003) and reflects that for a peak response component to be observed, the rate of binding and activation must be sufficiently fast for a large fraction of the population of receptors to open simultaneously, before onset of desensitization.

Figure 2 near here

Concentration-dependence of response kinetics

We also analyzed a series of response parameters as a function of the glutamate concentration. Because of the low number of glutamate receptor channels in the outside-out

patches and the small responses at the lowest concentrations tested, we only included responses evoked by glutamate concentrations between 100 μM and 30 mM in the kinetic analysis. For short pulse application of glutamate, we analyzed the deactivation kinetics and the 20-80% rise time. For long pulse application of glutamate, we analyzed the desensitization kinetics (by fitting the decay with a single or a double exponential function) and the 20-80% rise time. As illustrated in Fig. 2, the concentration of glutamate had little influence on either deactivation τ (Fig. 2a), desensitization τ (Fig. 2b) or the relative amplitude contributions (when fitting the decay of desensitization with a double exponential function; Fig. 2c). For the 20-80% rise time there was a small reduction with increasing concentration of glutamate (Fig. 2d). These results are overall similar to those obtained for non-NMDA receptors in patches from cerebellar Purkinje cells (Häusser and Roth, 1997) where the authors found little influence of the glutamate concentration except at the very lowest concentrations, at which our responses were too small to be reliably analyzed.

Figure 3 near here

Concentration-response properties of glutamate receptors: equilibrium desensitization

There is evidence that glutamate might be present in the extracellular space between neurons and glial cells at concentrations sufficient to give rise to equilibrium (steady-state) desensitization of AMPA receptors (Häusser and Roth, 1997; Cavelier et al., 2005; Herman and Jahr, 2007; Tzingounis and Wadiche, 2007). Furthermore, we have previously found evidence for spill-over activation of glutamate transporters on axon terminals of rod bipolar cells presynaptic to AII amacrine cells (Veruki et al., 2006), suggesting that the microenvironment around the corresponding synapses is not isolated from the surrounding neuropil. Accordingly, we were interested in examining the steady-state desensitization properties of the AMPA receptors of AII amacrine cells.

To examine the equilibrium desensitization properties, outside-out patches were exposed to different concentrations (0.3 μM - 100 μM) of glutamate for 1.75 s prior to ultrafast application of a pulse of 3 mM glutamate (duration 100 ms). For each patch, we first measured a control response to 3 mM glutamate without pre-exposure to glutamate (i.e. with glutamate-free solution as the control solution in the theta tube). This response was also used

to normalize the responses obtained after pre-exposure to glutamate (Fig. 3a). To correct for rundown, responses to 3 mM glutamate following pre-exposure to different glutamate concentrations were interleaved with responses to 3 mM glutamate following exposure to glutamate-free control solution. Normalization was calculated relative to the response to 3 mM glutamate expected for the same point in time obtained by curve fitting to a linear function in the same way as described above. We obtained results for 14 outside-out patches, with each patch contributing data for pre-exposure to 1 - 3 test concentrations of glutamate and for each concentration, we averaged the (normalized) responses from 3 - 11 patches. The data points were fitted with Eq. 3, yielding values for IC_{50}, i.e. the concentration giving rise to half-maximal desensitization, of 10.5 μM and n_H of 0.838 (Fig. 3b).

Figure 4 near here

Non-stationary noise analysis of glutamate-evoked currents in outside-out patches

To estimate the apparent single-channel current and $P_{open,\,max}$ of AMPA receptors of AII amacrine cells when activated by physiologically relevant concentrations of glutamate, we employed non-stationary noise analysis of responses evoked by ultrafast application of brief (~1.2 ms) pulses of glutamate (3 mM) to outside-out patches. Fig. 4a shows three individual responses evoked by glutamate in the same patch, together with the superimposed ensemble mean response (Fig. 4c; n = 20 responses used for the analysis). Fig. 4b illustrates the corresponding differences between each individual response and the ensemble mean (Fig. 4c), used to calculate the ensemble variance (Fig. 4d). The variance *versus* mean plot (corresponding to the decay phase after the peak response) displayed a partially parabolic shape with the ensemble variance falling slightly at the highest values of mean response, corresponding to $P_{open} > 0.5$ (Fig. 4e). When the data points were fitted with Eq. 4, the apparent single-channel current was 1.4 pA, corresponding to an apparent single-channel chord conductance of 23 pS. The number of available channels was 34, corresponding to a $P_{open,\,max}$ at the peak inward current of 0.62 (Fig. 4e). The average single-channel chord conductance was 24.5 ± 2.7 pS (range 17.3 - 38.3 pS; n = 7 patches), the average number of available channels was 21.8 ± 5.0 (range 5.2 - 42.3), and the average $P_{open,\,max}$ was 61.3 ± 2.0% (range 54.1 - 70.2). For two patches (both with 20-80% rise time of the average response ≤ 400

μs) we obtained variance *versus* mean curves with apparent $P_{open,\ max} < 0.5$, precluding adequate curve fitting (with Eq. 4). This could suggest, however, that a $P_{open,\ max}$ of 61% represents an overestimate of the true value. The considerably lower value for P_{open} estimated in a previous study from our laboratory (~0.3) can be explained by the use of nucleated patches and a system with slower speed of solution application (Mørkve et al., 2002). The lower single-channel conductance reported in our previous study (15. 2 ± 2.9 pS) could be related to the use of 1 mM (as opposed to 3 mM) glutamate in that study if the receptors display multiple conductance levels and agonist concentration-dependent occupancy (cf. Rosenmund et al., 1998; Smith and Howe, 2000; Gebhardt and Cull-Candy, 2006).

Figure 5 near here

Development of kinetic models for AMPA-type glutamate receptor channels

Our understanding of the synaptic connections between postsynaptic AII amacrine cells and presynaptic rod bipolar cells (Singer and Diamond, 2003; Veruki et al., 2003, 2006; Snellmann et al., 2009, 2011; Mehta et al., 2013, 2014) and OFF-cone bipolar cells (Veruki et al., 2003) is still rudimentary at the microphysiological level. While rapid advances are being made with respect to understanding the detailed structure of the complex morphological relationships between e.g. rod bipolar cell axon terminals and arboreal dendrites of AII amacrines (Mehta et al., 2014), further progress in improving our understanding of structure-function relationships is hampered by the lack of an adequate kinetic model for the AMPA-type glutamate receptors of AII amacrines. Several kinetic models with varying complexity, i.e. number and interconnections between states, have been proposed for AMPA receptors expressed in different neurons, but none have so far been adapted or modified with the goal of reproducing the properties of the AMPA receptors expressed by AII amacrine cells. An added advantage for such simulations is that once the receptor properties have been generalized into a kinetic scheme, a receptor population can be stimulated with arbitrary concentration profiles of agonist, such as might occur in the complicated 3D environments of the synapses between rod bipolar cells and AII amacrine cells and between OFF-cone bipolar cells and AII amacrine cells.

We were particularly interested to see if two different, previously published, AMPA receptor kinetic schemes could be adapted for AMPA receptors expressed in AII amacrine cells, based on experimentally observed data (Veruki et al., 2003; this study). The first scheme is that of Häusser and Roth (1997), henceforth referred to as HR97, and was developed to model AMPA receptors of cerebellar Purkinje cells (Häusser and Roth, 1997; Momiyama et al. 2003). This scheme has successfully been used to develop a kinetic model for AMPA receptors expressed by different types of OFF-cone bipolar cells in ground squirrel retina (DeVries et al., 2006). The scheme is based on the one originally proposed by Jonas et al. (1993) for hippocampal CA3 pyramidal neurons and later modified by Geiger et al. (1999) for hippocampal basket cell interneurons. Whereas the kinetic scheme of Jonas et al. (1993) contained seven states, including one open state and two glutamate binding sites, Häusser and Roth (1997) extended the scheme with two additional (closed) states (C6 and C7; Fig. 5a) to reproduce the double-exponential desensitization observed for AMPA receptors in Purkinje cells, similar to that observed for AMPA receptors in AII amacrine cells (Veruki et al., 2003). The second scheme investigated is that of Robert and Howe (2003), henceforth referred to as RH03, which was developed to model heterologously expressed AMPA receptors. The RH03 model (Fig. 6a) contains a larger number of states (16) than the HR97 model (9), but is considered more realistic with four glutamate binding sites and three open states (O2, O3, and O4) with different conductances, consistent with experimental observations of multiple conductance levels in AMPA receptors (Rosenmund et al., 1998; Smith and Howe, 2000; Smith et al., 2003; Gebhardt and Cull-Candy, 2006). We optimized the rate constants of these two kinetic schemes for AII amacrine AMPA receptors by model fitting, during which we simulated the model responses evoked by the same kind of agonist stimuli that were used in physiological experiments with application of glutamate to outside-out patches in our laboratory (Veruki et al., 2003; Table 2).

Figure 6 near here

Table 2 near here

To reduce the number of free parameters in the HR97 model, we calculated three rate constants, one for each cycle in the kinetic scheme (Häusser and Roth, 1997; Fig. 5a), from the other rate constants in the same cycle. This was done by adhering to the principle of

microscopic reversibility (Hille, 2001), such that the products of the rate constants in both directions (clockwise and counterclockwise) of each cycle were identical (Colquhoun et al., 2004). Without additional constraints, however, the fitting procedure for the HR97 model obtained a rate constant for glutamate unbinding from the doubly liganded state (k_{C2C1}; Fig. 5a) that was ~800 times faster than that for unbinding from the singly liganded state (k_{C1C0}; Fig. 5a), which is unrealistic. Therefore, we further constrained the rate constants of binding and unbinding of glutamate to the two sites in the model, reasoning that the following relationships should approximately hold (physical interpretations are indicated in parentheses):

$k_{C0C1} = 2 \times k_{C1C2}$	(glutamate binds to the two sites with equal rates and independently, i.e. no cooperative binding)
$k_{C1C0} = k_{C2C1} / 2$	(glutamate unbinds from the two sites with equal rates and independently)
$k_{C3C4} = k_{C1C2}$	(glutamate binds to the single-liganded states with equal rate constants irrespective of whether the states are desensitized or not)
$k_{C4C3} = k_{C2C1} / 2$	(in the desensitized state, one glutamate molecule is trapped whereas the other unbinds with the rate constant for unbinding from the doubly liganded, non-desensitized state)

These relationships were enforced either as soft constraints by adding the $\log_{10}$ of the ratios of the above left-hand and right-hand sides to the total error, or as hard constraints by calculating k_{C0C1}, k_{C1C0}, k_{C3C4} and k_{C4C3} from k_{C1C2} and k_{C2C1}. We compared the results of the model optimization without (additional) constraints to those obtained with either of these two types of additional constraints by assessing the RMS of the normalized deviations.

As expected, the best fits were obtained without additional constraints imposed. In this case, the properties of the fitted model deviated from the experimental values with an RMS deviation of 0.35 SEs. However, as stated above, the best fit generated an unrealistic ratio of ~800 for the two unbinding rate constants (k_{C1C0} / k_{C2C1}). Imposing soft constraints on the binding and unbinding rates of glutamate only slightly decreased the goodness of fit,

with an RMS deviation of 0.48 SEs. Importantly, none of the fitted properties displayed any marked deviation compared to the unconstrained model fitting and none of the above-mentioned relationships for the binding and unbinding rates deviated more than by a factor of ~10. When we imposed hard constraints, this strongly reduced the goodness of fit, with an RMS deviation of 1.4 SEs. Arguably these fits were still acceptable, but the average deviations were too large to be explained simply by experimental errors. Based on these results, the fits obtained from the softly constrained model seemed optimal, with only slightly increased deviations from the experimental observables and reasonable ratios for the binding and unbinding rates of glutamate. The corresponding rate constants are indicated in Fig. 5 (legend).

Figure 7 near here

Model fitting to the RH03 model was also performed to reproduce the experimentally observed response properties as closely as possible. The rate constants were constrained as suggested by Robert and Howe (2003; see Fig. 6a), taking into account molecular mechanisms of AMPA receptors. This included calculating the rate constant k_{-2} from the other constants in the cycle containing the ground state (Fig. 6a), based on considerations of microscopic reversibility (Hille, 2001). The properties used to fit the model contain no information concerning the absolute magnitudes of the single channel conductances, i.e. multiplying all conductances by the same factor would result in the same properties. We therefore used normalized values for the conductances of the open states and set the largest conductance (γ_{O4}; Fig. 6a) to 1. The model responses were simulated in the same way as was done for fitting to the HR97 model, with two notable changes. First, the model's response, i.e. the normalized current (analogous to P_{open} for the HR97 model) was calculated as the sum of the state occupancies (P) of the three open states multiplied by their (normalized) conductances ($P_{O2} \times \gamma_{O2} + P_{O3} \times \gamma_{O3} + P_{O4} \times \gamma_{O4}$). Second, to account for the presence of multiple open states with different conductances, an apparent $P_{open,\,max}$ was calculated by a procedure similar to that used for the experimental data (see Materials and methods) and is illustrated for clarity in Fig. 7. First, the average occupancies (Fig. 7a) of the individual open states during a step response were calculated from the model and the corresponding average current (Fig. 7b). From these results, the variance of the current was calculated (Fig. 7c).

Finally, the variance was resampled at evenly spaced time intervals and fitted with Eq. 4 to obtain apparent values for N, i and $P_{open,max}$ (Fig. 7d; see Materials and methods).

Initially, we let the conductances γ_{O2} and γ_{O3} be tuned by the optimization algorithm. However, this resulted in a near zero conductance of the corresponding states O2 and O3, resulting from an attempt of the optimization routine to increase the model's $P_{open, max}$. We considered this unlikely, given the published observations of multiple conductance levels for AMPA receptors (Rosenmund et al., 1998; Smith and Howe, 2000; Smith et al., 2000; Gebhardt and Cull-Candy, 2006). Therefore, the two conductances were set to fixed values of 0.333 (γ_{O2}) and 0.667 (γ_{O3}), using ratios observed for GluA4 homomeric receptors (Robert and Howe, 2003).

With the weights used for optimizing the HR97 model, the optimization routine was unable to obtain acceptable fits for the RH03 model (RMS deviation > 2 SEs). We found that the model could only closely reproduce the experimentally observed $P_{open, max}$ when the values for EC_{50}, maximum desensitization and rise time (Table 2) deviated markedly from the experimentally observed values (> ~3 SEs). To obtain acceptable fits to the other properties, while still obtaining a reasonable $P_{open, max}$ of ~0.5 or larger, we decreased the weight for $P_{open, max}$ by a factor of 2. This resulted in an optimized model (Fig. 6) with a $P_{open, max}$ of 0.47 and an RMS deviation for the other properties of 1.27 SEs, with no marked deviation from the experimentally observed values for any single property (Table 2). It is to be expected that the RH03 model was not able to fit the data as closely as the HR97 model, since it has far fewer free parameters to fit (10, compared to 19 for the HR97 model).

Responses of kinetic models to pulses and synaptic waveforms of glutamate

Next, we used the two kinetic models fitted to the AMPA receptors of AII amacrine cells (henceforth termed AII-HR97 and AII-RH03) to simulate responses to glutamate pulses of varying concentration and duration, as well as to hypothetical glutamate concentration profiles evoked by release of single synaptic vesicles into a synaptic cleft. To mimic synaptic glutamate concentration profiles, we used an instantaneously rising function with a double-exponential decay (parameters τ_1 = 0.1 ms, A_1 = 3 mM, τ_2 = 1 ms, A_2 = 0.5 mM), estimated from experimental measurements using low-affinity antagonists (Clements et al., 1992;

Clements, 1996; Diamond and Jahr, 1997; Scimemi and Beato, 2009) and from Monte Carlo simulations of glutamate release and diffusion in the synaptic cleft of a retinal ribbon synapse (Sikora et al., 2005). Since the parameters of the AII-HR97 and AII-RH03 models were fitted to reproduce the same data, their responses were very similar, both with respect to brief and long pulses of varying concentration and fixed-concentation pulses of varying duration (Fig. 5b, 6b). Both models generated responses that closely mimicked the responses obtained with outside-out patches (Fig. 1, Table 2). When stimulated with glutamate concentration profiles that mimicked release of single synaptic vesicles, both models generated similar responses (Fig. 5c, 6c) with kinetic characteristics resembling those of spontaneous excitatory postsynaptic currents (spEPSCs) recorded in AII amacrines (e.g. Veruki et al., 2003). When stimulated with a glutamate concentration profile that mimicked release of 10 synaptic vesicles in rapid succession (500 Hz), the responses generated by the two models differed slightly in the kinetics of the onset and around the peak (Fig. 5c, 6c).

Figure 8 near here

Non-stationary noise analysis of responses generated by kinetic models of AII amacrine AMPA receptors

Non-stationary noise analysis can be used to estimate the single-channel current, the $P_{\text{open, max}}$ and the number of available channels involved in mediating the response to agonist application (see above; for review, see Hartveit and Veruki, 2007). However, the presence of quantal variablity complicates the use of conventional non-stationary noise analysis. Peak-scaled non-stationary noise analysis was introduced to compensate for the quantal variability (Traynelis et al., 1993), but the resulting variance *versus* mean relationships can be transformed from parabolic to skewed (Momiyama et al., 2003; Hartveit and Veruki, 2006, 2007). In that condition, fitting with Eq. 4 to a range of the variance *versus* mean relationship can still be used to obtain an estimate for the single-channel current, but the estimate for N has no physical interpretation. In a previous study from our laboratory, we investigated a series of different kinetic schemes for neurotransmitter receptor channels and demonstrated that the shape of the variance *versus* mean relationships is a consequence of the temporal structure of the fluctuations of the ion channel gating during the responses (Hartveit and

Veruki, 2006). Specifically, covariance analysis indicated that peak-scaling generates a skewed relationship when the covariance function decays rapidly and a parabolic relationship when it decays more slowly. In each case, the decay of the covariance function is compared to the decay of the average response waveform. Rapid decay or slow decay means that there is low or high correlation between fluctuations at the peak and during the decay phase, respectively.

We next investigated these properties for the two different kinetic schemes developed for AMPA receptors of AII amacrine cells, using stochastic simulations to generate an ensemble of responses (n = 1000 events) evoked by 1 ms square-wave pulses of five different concentrations of glutamate (0.3, 1, 3, 5, and 100 mM). For the AII-HR97 kinetic scheme (Fig. 5a), we obtained variance *versus* mean relationships that closely followed the expected theoretical relationship predicted by Eq. 4, and for the three highest concentrations, $P_{\text{open, max}}$ was > 0.5 (Fig. 8a). For each concentration of glutamate, estimates for i and N were obtained by fitting with Eq. 4. We estimated the statistical errors in two different ways, first by repeating the stochastic simulations 10 times (n = 1000 events in each ensemble) and then by analyzing 100 bootstrap "synthetic" data sets re-sampled from one of the original data sets (see Materials and methods for details). The results displayed in Table 3 indicated that overall both procedures generated similar error estimates (both for i and N). The coefficient of variation (CV) was typically between 5 and 10% and the bias was typically <5%. As expected, the CV for estimates of N at the lowest glutamate concentrations (0.3 and 1 mM) were considerably larger, corresponding to a $P_{\text{open, max}} < 0.5$ (Fig. 8a).

To mimic a source of quantal variability, we repeated the simulations with stochastic variation of the number of available channels from trial to trial. As expected, the stochastic variation of the number of available channels increased the variance (for a given mean response value) over that generated by the stochastic channel gating itself and the resulting variance *versus* mean curves deviated strongly from a parabolic shape (Fig. 8b). It was still possible to obtain a good estimate for i by fitting the initial part of the curve with a straight line, in which case the CV was < 5% and the bias was < 7% (Table 3). When we compensated for the increased variability caused by the stochastic variation in the number of available channels by scaling the peak of the ensemble mean to each individual response before

calculating the difference traces (cf. Fig. 5), the variance was strongly reduced (Fig. 8d). Although the variance *versus* mean relationships became somewhat skewed, the peak scaling almost perfectly adjusted the variance *versus* mean relationships such that they followed the theoretical relationship predicted by Eq. 4 (Fig. 8d). As observed previously for other kinetic schemes (Hartveit and Veruki, 2006), the variance *versus* mean relationships generated by peak scaling were observed irrespective of whether the responses were generated with a constant or variable number of available channels (Fig. 8c, d). By excluding the rightmost points of the variance *versus* mean relationships, curve fitting with Eq. 4 yielded good estimates not only of i (for all glutamate concentrations), with CV around 5% and bias < 4% (Table 3), but for the three highest glutamate concentrations (3, 5 and 100 mM), the estimates for N corresponded to the average number of available channels (cf. Fig. 8c, d), with CV typically between 5 and 10% (Table 3).

We also performed non-stationary noise analysis of simulated responses based on the kinetic scheme derived from the Robert and Howe (2003) model (AII-RH03). In this model, the ion channels have concentration-dependent, multiple conductance levels and this is implemented as multiple, non-identical open states corresponding to doubly, triply and quadruply liganded states (O2, O3 and O4, respectively; Fig. 6a). In the original model the three open states were assigned single-channel conductances of 8, 16 and 24 pS, respectively (Robert and Howe, 2003). When we fitted our experimental results to the RH03 model, we were not able to assign absolute conductance values to the different open states, and set the relative conductance values to 0.333, 0.667 and 1 for the doubly, triply and quadruply liganded states, respectively. Here, when we set the absolute conductance values for these states to 12, 24 and 36 pS, respectively, non-stationary noise analysis of simulated responses evoked by brief (1.2 ms; 20-80% rise and decay time 0.25 ms) pulses of 3 mM glutamate generated an apparent single-channel conductance similar to that obtained experimentally in outside-out patches (Table 2).

With stochastic simulations to generate ensembles of responses (n = 1000 events) evoked by 1 ms square-wave pulses of five different concentrations of glutamate (0.3, 1, 3, 5, and 100 mM), we obtained variance *versus* mean curves that followed intermediary paths compared to those predicted from Eq. 4 and the three different single-channel conductances

(Fig. 8e). Overall, the curves were closest to the theoretical relationship predicted by the intermediate open state with single-channel conductance of 24 pS, but the curve generated with 100 mM glutamate followed the theoretical relationship corresponding to the highest conductance at the largest values of mean current (Fig. 8e). Importantly, when the variance *versus* mean relationships in Fig. 8e were fitted with Eq. 4, we obtained larger values of apparent single-channel current (*i*) with increasing concentration of glutamate (Table 4). The concentration-dependent increase of the estimated value for the apparent unitary current (*i*) is likely to correspond to increasing occupancy of the higher conductance states with increasing glutamate concentration (Rosenmund et al., 1998; Smith and Howe, 2000; Smith et al., 2000; Gebhardt and Cull-Candy, 2006).

When we repeated simulations and varied the number of available channels stochastically, the variance *versus* mean curves deviated strongly upwards (Fig. 8f). A linear fit to the initial part of the curve resulted in concentration-dependent estimates of *i* ranging from ~1.0 to ~1.5 pA (Table 4). When we applied peak scaling to the non-stationary noise analysis, the variance *versus* mean curves were moderately skewed (irrespective of whether peak scaling was applied to simulations with constant or variable number of available channels (Fig. 8g, h). With peak scaling, the estimates for *i* were slightly lower than those obtained without peak scaling, for a given concentration of glutamate, but still increased with increasing concentration of glutamate (Table 4).

Figure 9 near here

Covariance analysis of responses generated by kinetic models of AII amacrine AMPA receptors

To understand the consequences of peak scaling and the generation of skewed variance *versus* mean relationships during non-stationary noise analysis, it can be useful to calculate the covariance functions for the response ensembles (Hartveit and Veruki, 2006). The coveriance function (in the time domain) characterizes how well the fluctuations are correlated at different times and is equivalent to the power spectral density function in the frequency domain (e.g. Bendat and Piersol, 2000). We were particularly interested to see how the covariance functions for responses simulated with either of the two different kinetic

schemes developed for AII amacrine AMPA receptors compared with each other and with the same kind of functions calculated from experimental responses using outside-out patches.

To mimic the experimental conditions, the simulations used pulses of glutamate (3 mM, 1 ms duration) with finite rise and decay times (20-80% rise and decay times of 0.25 ms; Fig. 9a, d). Each covariance function was calculated from 1000 repetitions. Apart from a difference in absolute magnitude, the covariance functions for the two sets of responses simulated with either the AII-HR97 or the AII-RH03 kinetic schemes were relatively similar (Fig. 9b, e). We also analyzed the corresponding correlation functions with center point set to the peak of the mean response waveform (Fig. 9c, f; red traces). For both AII-HR97 and AII-RH03, the correlation functions displayed an initial component with extremely fast decay, most pronounced for AII-RH03 (Fig. 9f). Following this component, the decay of both correlation functions could be fitted with a single exponential function, with a time constant of 1.1 ms for both AII-HR97 and AII-RH03. The time constants of deactivation for the corresponding mean responses were approximately the same (Fig. 9a, d; Table 2). For three outside-out patches, we obtained a sufficiently large number of responses under stable conditions without rundown to allow calculation of covariance functions with reasonably low noise. The single-exponential time constants of decay of the correlation functions (with center point at the peak of the mean) were 1.0 (Fig. 9i; red trace), 0.8 and 0.5 ms. The deactivation time constants for the ensemble mean responses for the same patches were 1.1 (Fig. 9g), 0.7 and 0.9 ms, respectively. The similarity between the time constants of the decay of the correlation function and the deactivation of the mean response most likely explains why peak scaling only gives rise to moderately skewed variance *versus* mean relationships (Fig. 8c, d, g, h). When we applied peak scaling to the non-stationary noise analysis of the responses obtained in outside-out patches, the results were fairly similar, with the variance *versus* mean relationship approximately skewed for two patches, approximately parabolic for two patches and intermediary for three patches. In summary, both of our kinetic models are able to reproduce an extensive set of specific functional properties of AMPA receptors of AII amacrine cells.

Figure 10 near here

Association of the GluA4 subunit with glutamatergic input to both arboreal and lobular dendrites of AII amacrine cells

Certain functional properties (kinetics of deactivation, desensitization and recovery from desensitization) of homomeric glutamate receptors composed of the flip variant of the AMPA receptor GluA4 subunit are very similar to those observed for glutamate receptors in outside-out patches of AII amacrine cells (Veruki et al., 2003). Interestingly, immunocytochemical investigations, both at the light and electron microscopic level, have suggested the location of GluA4, as well as GluA3, but not GluA1 or GluA2, in the synapses made by rod bipolar cells on the arboreal dendrites of AII amacrine cells (cat: Qin and Pourcho, 1999; rabbit: Ghosh et al., 2001; Li et al., 2002; monkey: Ghosh et al., 2001). In addition to input from rod bipolar cells at the arboreal dendrites, however, AII amacrine cells also receive input from some types of OFF-cone bipolar cells targeted to the lobular dendrites and the lobular appendages (Kolb and Famiglietti, 1974; Strettoi et al., 1992; Chun et al., 1993). Very little is known with respect to the glutamate receptors that mediate input from OFF-cone bipolar cells to AII amacrine cells, except that they are likely to correspond to AMPA receptors, as all spEPSCs can be blocked by AMPA receptor-selective antagonists (Veruki et al., 2003) and kainate receptors have not been detected on these cells (Mørkve et al., 2002). In addition, in recordings of spEPSCs from AII amacrine cells, there is no evidence for any heterogeneity that would suggest two distinct populations of spEPSCs corresponding to synaptic input from rod and OFF-cone bipolar cells, respectively (Veruki et al., 2003). Because the GluA4 subunit seems to play an important role for the functional properties of AMPA receptors in AII amacrines and seems to be expressed in synapses made by rod bipolar cells in other species, we focused on the potential location of this AMPA receptor subunit to elucidate the properties of the synaptic input not only from rod bipolar cells to the arboreal dendrites, but also from OFF-cone bipolar cells to the lobular dendrites and appendages of AII amacrines.

To examine the relationship between GluA4 expression and processes of AII amacrine cells, we acquired confocal image stacks of slices with cells injected with Alexa 488 and immunolabeled for GluA4 (Fig. 10a). We observed strong, punctate labeling of GluA4

across the inner plexiform layer, with roughly similar density of punctae in sublaminae *a* and *b*, consistent with previous results for cat, rabbit and monkey retinae (Qin and Pourcho, 1999; Ghosh et al., 2001). It is generally assumed that each fluorescently labeled punctum corresponds to a cluster of receptors, potentially corresponding to a synaptic location. Visual inspection of single slices of the confocal stack, with both channels (AII and GluA4) overlaid, identified several examples of GluA4 punctae that overlapped with the AII amacrine cell, both for lobular processes in sublamina *a* (Fig. 10b) and for arboreal processes in sublamina *b* (Fig. 10c).

For a quantitative, object-based colocalization analysis (Bolte and Cordelières, 2006; Dunn et al., 2011), we used simple threshold segmentation to identify structures in both the AII channel and the GluA4 channel. Following segmentation, we isolated all segmented GluA4 objects that overlapped (intersected) with structures belonging to the segmented AII amacrine cell. Although the physiological experiments with outside-out and nucleated patches indicate that AMPA receptors are present at the cell body of AII amacrine cells, there is no evidence for input from bipolar cells directly onto the cell body of AII amacrine cells (e.g. Tsukamoto and Omi, 2013). In addition, the fluorescence intensity of the cell body was very high and with simple threshold segmentation that captures as many as posible of the thinner processes of AII amacrine cells, the cell body will typically be considerably over-segmented. Accordingly, this region was excluded from the morphological analysis. By chance, some punctae will most likely overlap with AII processes without having a synaptic relationship to the same cell. This means that the total population of overlapping GluA4 punctae is likely to include false positives when the minimum criterion for being classified as overlapping was sharing a single voxel between the segmented volumes of a GluA4 punctum and an object belonging to the segmented AII amacrine. However, with adequate immunolabeling it is highly likely that the population of overlapping punctae will include punctae representing synaptic receptor clusters. For the AII amacrine illustrated in Fig. 10, a total of 167 GluA4 objects overlapping with AII processes were detected (Fig. 10d). For each overlapping GluA4 object we analyzed the distance from its intensity-weighted center of mass (CM) to the nearest point of the surface of the segmented AII amacrine cell and the relative fraction of the object (punctum) volume that was occupied by the AII amacrine (as a

measure of colocalization), illustrated by the histograms in Fig. 10e and 10f, respectively. For 94 of the overlapping punctae, the CM-to-surface distance was ≤100 nm, suggesting that the punctae could correspond to synaptic clusters on the AII amacrine. For 37 of the overlapping punctae, the relative colocalization was ≥50% (Fig. 10d), also suggesting that the punctae could correspond to synaptic clusters. Plotting the relative colocalization *versus* the CM-to-surface distance, indicated that when the colocalization increased from 0 to 50% the CM-to-surface distance decreased and that when the colocalization increased from 50 to 100% the surface distance slightly increased again (Fig. 10g), most likely because the CM of the corresponding punctae was located on the inside of the segmented AII structures and further from the surface.

Fig. 11 near here

For a total of eight AII amacrine cells, the average number of overlapping punctae was 402 ± 61 (range 167 - 684). The average number of punctae with CM-to-surface distance ≤100 nm was 190 ± 36 (range 60 - 362) and the average number of punctae with relative colocalization ≥50% was 132 ± 21 (range 38 - 218). Fig. 11 shows the distribution of the number of punctae with relative colocalization ranging between >0 and 100%, plotted for overlap increments of 10%, for all eight AII amacrine cells. When we increase the criterion for genuine colocalization between an overlapping GluA4 punctum and an object belonging to the AII amacrine higher than >0%, the number of false positives will decrease, but at the same time the number of false negatives will increase, i.e. we are likely to miss some GluA4 punctae that are genuinely located at the process of the AII cell.

We next extracted the average signal in the AII channel in a volume corresponding to a square prism surrounding the CM coordinates of all GluA4 punctae that overlapped with the segmented AII amacrine cell. As a control, we also performed the same analysis for the signal in the GluA4 channel itself. Fig. 10h shows the central slice and corresponding line profile through the averaged signal in the GluA4 channel around the spatially aligned CM coordinates of the GluA4 punctae that overlapped with the AII amacrine, essentially displaying the point spread function of the imaging system in the XY plane (assuming that the signal source of each GluA4 punctum is too small to be resolved by light microscopic imaging as used here). The corresponding average signal in the AII channel around the CM

coordinates for the overlapping GluA4 punctae is shown in Fig. 10i and indicated a clear increase above background. When we repeated the same analysis separately for overlapping punctae located in sublamina *a* (n = 64 punctae) or *b* (n = 103 punctae; sublaminae *a* and *b* demarcated from each other by the location of the arrow head in Fig. 10a), both regions displayed increased signal from the AII amacrine around the overlapping GluA4 punctae (Fig. 10j, k). For the lobular dendrites, the signal in the AII channel displayed a broad profile (Fig. 10j), corresponding to the thicker lobular dendrites and appendages. For the arboreal dendrites, the signal in the AII channel displayed a narrow profile (Fig. 10k), corresponding to the overall thinner arboreal processes. When we repeated this analysis by including only the CM coordinates of GluA4 punctae with ≥50% overlap, the results were qualitatively very similar, both for the average signal in the AII channel as a whole (n = 38 punctae; Fig. 10l) and when we performed the analysis separately for overlapping punctae located in sublamina *a* (n = 17 punctae; Fig. 10m) or *b* (n = 21 punctae; Fig. 10n).

Figure 12 near here

If the GluA4 punctae overlapping with the AII amacrine cell correspond to synaptic clusters of receptors, it is expected that they should be spatially correlated with the presence of the postsynaptic scaffold protein PSD95 (Ghosh et al., 2001) and presynaptic ribbon proteins like ribeye (Schmitz et al., 2000; Lagnado and Schmitz, 2015). To investigate this, retinal slices with injected AII amacrine cells were double immunolabeled with antibodies against either GluA4 and PSD95 or GluA4 and CtBP2 (identical with the B domain of ribeye; Schmitz et al., 2000). The maximum intensity projection of the AII amacrine cell illustrated in Fig. 12a is from a slice immunolabeled for GluA4 and PSD95. Visual inspection of single slices in the confocal stack identified several examples of apparent overlap between the AII amacrine and GluA4 with associated punctate labeling for PSD95, both in the lobular region (sublamina *a*; Fig. 12b) and arboreal region (sublamina *b*; Fig. 12c). We then used the CM coordinates of the GluA4 punctae overlapping with the AII amacrine (n = 500 punctae) to estimate the average signal in and around the punctae, both in the AII channel and in the PSD95 channel. The presence of a GluA4 punctum resulted in a localized signal increase above background not only in the AII channel (similar to Fig. 10i-k), but also in the PSD95 channel, strongly suggesting that clusters of GluA4-containing receptors are associated with

PSD95 (Fig. 12d). The correlation between GluA4 and PSD95 was also observed when we repeated the analysis separately for overlapping punctae located in sublamina *a* (n = 154 punctae) or *b* (n = 346 punctae; sublaminae *a* and *b* demarcated from each other by the location of the arrow head in Fig. 12a), with increased PSD95 signal around the overlapping GluA4 punctae both for lobular (Fig. 12e) and arboreal processes (Fig. 12f). When we repeated the analysis by including only the CM coordinates of GluA4 punctae with ≥50% overlap, the results were qualitatively very similar, both for the average signal in the PSD95 channel as a whole (n = 149 punctae; Fig. 12g) and when we performed the analysis separately for overlapping punctae located in sublamina *a* (n = 38 punctae; Fig. 12h) or *b* (n = 111 punctae; Fig. 12i). This suggests that AMPA receptors involved in mediating input to AII amacrine cells from OFF-cone bipolar cells and rod bipolar cells both contain the GluA4 subunit and are likely to have similar functional properties. Virtually identical results were observed for another injected AII amacrine cell in a slice labeled for GluA4 and PSD95. These results reflect the average signal of PSD95 associated with a GluA4 receptor cluster on an AII amacrine cell. When we manually examined the confocal stack, we also found several examples of GluA4 punctae that did not seem to be closely associated with a cluster of PSD95 labeling (e.g. Fig. 12b, c).

Figure 13 near here

The colocalization of AII amacrine-associated GluA4 receptor clusters with PSD95 suggested that these receptors are generally located at synapses. A synaptic location predicts that the GluA4 punctae should also be associated with ribbon proteins located in the corresponding presynaptic bipolar cells. Thus, we also examined retinal slices with dye-injected AII amacrine cells and double immunolabeled for GluA4 and CtBP2. Fig. 13a shows maximum intensity projections of an AII and fluorescently labeled punctae of GluA4 and CtBP2. Visual inspection of single slices in the confocal stack identified several examples of apparent overlap between the AII amacrine, GluA4 punctae and CtBP2 punctae, both in the lobular region (sublamina *a*; Fig. 13b) and arboreal region (sublamina *b*; Fig. 13c). When the CM coordinates of the GluA4 receptor clusters overlapping with the AII amacrine cell (n = 377 punctae) were used to extract the average signal in the AII amacrine and CtBP2 channels, we observed increased signal not only for the AII amacrine (similar to Fig. 10i-k), but also for

CtBP2 (Fig. 13d). When the population of overlapping GluA4 punctae was divided into two groups corresponding to lobular processes in sublamina *a* (n = 85 punctae; Fig. 13e) and arboreal dendrites in sublamina *b* (n = 292 punctae; Fig. 13f; sublaminae *a* and *b* demarcated from each other by the location of the arrow head in Fig. 13a), both populations displayed enhanced signal for CtBP2. When we repeated the analysis by including only the CM coordinates of GluA4 punctae with ≥50% overlap, the results were qualitatively very similar, both for the average signal in the CtBP2 channel as a whole (n = 154 punctae; Fig. 13g) and for overlapping punctae located in sublamina *a* (n = 28 punctae; Fig. 13h) or *b* (n = 126 punctae; Fig. 13i). These results suggest that clusters of GluA4 receptors associated with both lobular and arboreal dendrites of AII amacrine cells are postsynaptic at ribbon synapses of bipolar cells. Similar results were seen for a second AII amacrine cell injected in a slice immunolabeled for GluA4 and CtBP2.

Discussion

Understanding synaptic transmission at ribbon synapses requires a knowledge of both the presynaptic machinery specialized for releasing synaptic vesicles at high rates for extended periods of time, as well as how the postsynaptic receptors translate the spatiotemporal concentration profiles of glutamate into electrical signals. In this study we used an extensive series of experimental observables to develop kinetic models for AMPA receptors of AII amacrine cells. Such models are essential for developing realistic computational models to explore synaptic signaling at the nanoscale level. We verified the ability of these kinetic models to reproduce a series of experimental results and explored the models' behavior in relation to simple glutamate concentration profiles and conditions of physiological relevance. In addition, we investigated the molecular basis for the unique properties of AMPA receptors of AII amacrine cells with a focus on the GluA4 subunit. Using immunolabeling, we demonstrated that this subunit was present not only at synapses made by rod bipolar cells, but also at synapses from OFF-cone bipolar cells. This suggests that AMPA receptors at both synaptic locations use similar mechanisms to adapt their functional properties to respond to ribbon synapse release patterns.

Functional properties of AMPA receptors of AII amacrine cells and adaptation to ribbon synapses

We now have extensive quantitative information about the functional properties of AMPA receptors expressed in AII amacrine cells. This includes information about Ca^{2+} permeability, activation kinetics, deactivation kinetics, kinetics and extent of desensitization, kinetics of recovery from desensitization, concentration-response properties, concentration dependence of equilibrium desensitization, $P_{open,\,max}$, and single-channel conductance (Mørkve et al., 2002; Singer and Diamond, 2003; Veruki et al., 2003; this study). For AMPA receptors at ribbon synapse input to AII amacrines, two properties seem to be of particular relevance: the IC_{50} for equilibrium desensitization and the fast recovery from desensitization.

First, the IC_{50} of 10.5 μM for equilibrium desensitization is relatively similar to observations made for AMPA receptors in neurons with action potential-mediated glutamatergic input, such as cerebellar Purkinje cells (8.7 μM; Häusser and Roth, 1997) dentate gyrus basket cells (2.2 μM; Geiger et al., 1999) and hippocampal (CA3) pyramidal neurons (9.6 μM; Colquhoun et al., 1992). It is difficult, however, to predict the functional consequences of these values for the transmission in specific synapses. The extent to which synaptic receptors undergo steady-state desensitization will depend both on the time-averaged vesicle release rates, which can vary considerably between synapses, as well as on the clearance rate of glutamate after release into the synaptic cleft. The clearance could depend strongly on the ultrastructure and synaptic environment, either promoting or preventing pooling of neurotransmitter at concentrations giving rise to steady-state desensitization. In addition, the extent to which the microenvironment of postsynaptic densities is protected from ambient glutamate via ensheathment by glial cell membranes seems to be highly variable and region-specific. In other regions of the central nervous system, the ambient concentration of glutamate in the extracellular space is uncertain, with estimates ranging from ~0.02 to ~20 μM (Herman and Jahr, 2007; Moussawi et al., 2011), but to our knowledge similar estimates for the retina are not available. This remains an important goal for future investigations.

Second, whereas the AMPA receptors of AII amacrines display fast and extensive desensitization and a glutamate-sensitivity of equilibrium desensitization that is similar to

that observed for other AMPA receptors, the recovery from desensitization is surprisingly fast, with $\tau_{recovery}$ ~13 ms (Table 2). This property is likely to be of particular importance for enabling the postsynaptic AMPA receptors to continue to respond to glutamate even when vesicles are released continuously at a high rate. For rod bipolar cells, the maximum sustained release rate at an individual release site (ribbon) can be estimated to be approximately 30 - 45 Hz (see Oltedal and Hartveit, 2010 for a discussion). For OFF-cone bipolar cells, we are not aware of corresponding estimates. For several other neurons, the kinetics of recovery from brief-pulse desensitization of AMPA receptors is typically much slower. In Purkinje cells, $\tau_{recovery}$ is ~33 ms (Häusser and Roth, 1997), in dentate gyrus basket cells the recovery is bi-exponential with time constants of 34 and 387 ms (Koh et al., 1995), and in CA3 pyramidal neurons $\tau_{recovery}$ is ~48 ms (Colquhoun et al., 1992). Few neurons express AMPA receptors with recovery almost as fast as for the AMPA receptors of AII amacrines. One example is for neurons in the chick nucleus magnocellularis ($\tau_{recovery}$ ~16 ms; Raman and Trussell, 1995). Another example is for a particular type of OFF-cone bipolar cell in tree shrew retina (b2, $\tau_{recovery}$ ~18 ms; DeVries, 2000). Other types of OFF-cone bipolar cells investigated in the same study displayed much slower recovery, suggesting that fast recovery is not a general characteristic of AMPA receptors at ribbon synapses. The kinetic models developed in the present study will allow detailed computational exploration of the functional consequences of the fast recovery from desensitization for the synaptic transmission between bipolar cells and AII amacrine cells.

A limitation of this and most other kinetic models for receptor channels expressed by specific neurons is that because synaptic receptors are typically located in the dendrites, their kinetic properties are difficult to investigate. For technical reasons, most of the kinetic properties are therefore measured in experiments with membrane patches that allow activation by ultrafast application of agonist to mimic the temporal concentration profile of neurotransmitter in a chemical synapse (Clements, 1996). Except for a relatively small number cases when neuronal processes are thick enough to permit excision of outside-out patches, most investigations have employed somatic patches. Such patches may have a different subunit composition and may exist in association with different accessory proteins or cytoskeletal elements than the synaptic receptors (for a discussion, see Hartveit and

Veruki, 2007). For AII amacrine cells, there is no evidence for synaptic input from bipolar cells directly onto the cell body and the receptors that are located there must be considered extrasynaptic. However, for kinetic parameters that can reasonably be compared for synaptic and extrasynaptic receptors (e.g. the decay time constants of spEPSCs and brief pulse patch responses), the properties of extrasynaptic (somatic) and synaptic AMPA receptors of AII amacrine cells seem to be reasonably similar (see Veruki et al., 2003, for a detailed discussion).

Kinetic modeling

Early kinetic models of AMPA receptors assumed that each receptor had two binding sites which both had to be occupied for the channel to open. However, there is strong evidence that AMPA receptors are tetramers and contain four binding sites for glutamate (reviewed by Plested, 2015). In addition, there is strong evidence that AMPA receptors show multiple conductance levels and that increasing occupancy increases the single-channel conductance (Rosenmund et al., 1998; Smith and Howe, 2000; Smith et al., 2000; Gebhardt and Cull-Candy, 2006). Here, we used ultrafast application of glutamate to outside-out patches to extend the functional characterization of AMPA receptors of AII amacrine cells, enabling us to generate computational models in the form of Markov-type kinetic schemes. Rate constants were obtained by model fitting to reproduce the experimental data. Such models are not only a compact representation of the dynamic properties of the receptor channels (cf. Häusser and Roth, 1997), but also provide convenient and unique possibilities for computational modeling.

Typical for the kind of optimization problem involved in model fitting, the resulting rate constants were relatively poorly constrained. This was evidenced by the fact that the same local minimum (with a tolerance of 10%) was never obtained twice by the local optimization algorithm when simulations were started from > 300 random starting points. Accordingly, values of individual rate constants obtained in this way for a given model structure should not be compared between different types of receptors. More reliable determination of specific rate constants will require single-channel recording (Colquhoun and Hawkes, 1995), which has had limited success for AMPA receptors due to their

extremely fast kinetics. Nevertheless, the obtained kinetic models faithfully reproduce a series of experimental observables without any obvious erroneous properties and are thus succinct representations of the dynamics of the receptors that will enable *in silico* modeling and experimentation.

For two reasons, the EC_{50} and Hill coefficient for the steady-state concentration-response relationship were not used for model fitting. First, the steady-state responses are low even for nucleated patches and high concentrations of glutamate. For outside-out patches, the amplitude of the steady-state, non-desensitizing response is only ~4% of the peak amplitude. Second, the dependence of this response component on glutamate concentration is most likely not important for normal functioning of synaptic AMPA receptors. Accordingly, we chose not to fit the concentration-dependence of the steady-state conductance in favor of a better fit to other properties which are functionally more relevant.

Of the two models, the AII-RH03 incorporates our current understanding of the molecular structure of AMPA receptors with four binding sites, three open states and three conductance levels. This model fits the experimental observables only slightly worse than the AII-HR97 model, accordingly, we believe that the AII-RH03 model should be preferred for future *in silico* experiments. On the other hand, because the AII-HR97 model has fewer states and therefore is considerably faster computationally, it might be preferred for certain studies. With fewer states and an overall simpler structure, it is also easier to extend with additional states to accommodate experimental measurements of the effect of antagonists (e.g. Wadiche and Jahr, 2001).

It is a limitation of the kinetic models developed in this study that the physiological measurements were performed at room temperature (22 - 25 °C). The different processes and phenomena underlying synaptic transmission (transmitter diffusion, receptor kinetics, single-channel conductance, etc.) display marked dependence (roughly exponential) on temperature (for reviews, see Hille, 2001; Roth and van Rossum, 2010; Sterratt et al., 2011). The temperature dependence of synaptic kinetics is in general very steep, with a Q_{10} temperature coefficient (the experimentally determined change for a 10-degree difference in temperature) typically of about 2 - 3 (Roth and van Rossum, 2010). This is similar to the Q_{10} for time constants of activation and inactivation of voltage-gated ion channels (e.g. Destexhe

and Huguenard, 2010), rate coefficients of gating of ion channels, and many enzyme reactions (Hille, 2001). In contrast to gating, the (maximum) conductance of an open ion channel is considerably lower, with a Q_{10} of only 1.2 - 1.5 (similar to that for aqueous diffusion of ions; Hille, 2001). If the channel kinetic data were obtained at room temperature, but a model for the channel will be used at a higher temperature that is physiologically more relevant, the kinetic properties of the channel must be scaled accordingly. In the ideal case, the Q_{10} has been measured, but often this is not the case and one must resort to scaling by default values. One possibility is to scale all the reaction rate constants of the different transitions in a Markov-style model uniformly by the same multiplicative factor (corresponding to a specific value for Q_{10}; e.g. Postlethwaite et al., 2007). Unfortunately, this is not always appropriate, as there is evidence, at least for some receptor channels, that the Q_{10} for different transitions can differ substantially (Cais et al., 2008). Whereas we have not obtained estimates for the temperature-dependence of glutamate-evoked responses of receptors in patches from AII amacrine cells, our laboratory has previously published estimates for the Q_{10} of spEPSCs, with a Q_{10} of 1.5 for the τ_{decay}, 1.3 for the 10-90% rise time, and 1.4 for the peak amplitude (Veruki et al., 2003). The Q_{10} for τ_{decay} is similar to that found for cerebellar granule cells (1.7), but both values are lower than the Q_{10} for τ_{decay} of patch responses from cerebellar granule cells (Silver et al., 1996). It is possible that Q_{10} values for EPSC decay kinetics are underestimated because of electrotonic filtering that effectively sets a lower limit for the experimentally measured values.

Immunolabeling and morphological analysis of synaptic proteins

Because of previous evidence for involvement of the AMPA receptor subunit GluA4 in the synaptic input from rod bipolar cells to AII amacrine cells (Qin and Pourcho, 1999; Ghosh et al., 2001; Li et al., 2002) and the similarity between several functional properties of the AMPA receptors of AII amacrine cells and homomeric GluA4 receptors, we focused the morphological investigations on this subunit. Our analysis used immunolabeling for the GluA4 subunit in retinal slices with AII amacrine cells filled with fluorescent dyes. After threshold segmentation of the fluorescent cell and immunolabeled GluA4 punctae, we isolated all punctae that overlapped with an object belonging to the cell. As the minimum

criterion for overlap corresponded to sharing a single voxel, the population of GluA4 punctae isolated in this way is likely to include a number of false positives, i.e. punctae that do not correspond to a cluster of receptors located in the membrane of the dye-filled AII amacrine cell. In addition, our analysis also included overlap in the axial direction where resolution is lower (than in the lateral direction). When we graphed the number of overlapping GluA4 punctae as a function of the relative overlap with the AII amacrine, the number of overlapping punctae decreased smoothly as a function of overlap, with an average of 132 punctae with ≥50% overlap. This number will include fewer false positives, but is unfortunately likely to include a larger number of false negatives, i.e. it will have missed punctae corresponding to receptor clusters located in the cell membrane of the dye-filled cell. This can happen when a given process is undersegmented because of low intensity or when a GluA4 punctum is located at a particularly thin process such that the segmented volume of the process occupies a (relatively) small fraction of the segmented volume of the GluA4 signal.

A rough guide to the expected number of synaptic punctae might be found in the recent results obtained for AII amacrine cells in mouse retina with complete reconstructions of three cells from electron microscopic images (Tsukamoto and Omi, 2013). On average, the AII amacrines received input at 173 ribbon synapses. From the average relation between the relative overlap (colocalization) of a GluA4 punctum and the number of associated punctae in our light microscopic data, this would correspond to an overlap of about ≥40% (Fig. 11). For a considerable range of values for relative overlap between segmented GluA4 punctae and objects belonging to the segmented AII amacrine, there is considerable variability of the total number of overlapping GluA4 punctae between different AII amacrines, approximately 3- to 4-fold range (Fig. 11). Some of this variability could be explained by a corresponding variability of cell size. In a recent morphometric study from our laboratory (Zandt et al., 2017), we found that the length of the total arborization of AII amacrine cells varied over 3-fold (range 500 - 1630 μm). Although the presence of an overlapping GluA4 punctum predicted a locally increased intensity for both postsynaptic PSD95 and presynaptic ribbons (CtBP2), it is difficult to exclude the possibility that some of the GluA4 punctae could be extrasynaptic and corresponding to clusters of GluA4 receptors outside the PSDs of ribbon

synaptic input. It remains an important question to investigate the total number of ribbon synapses in AII amacrine cells, how it scales with cell size and the length of lobular and arboreal dendrites. This will require complete morphological reconstruction (cf. Zandt et al., 2017) and, ideally, validating the classification of overlapping punctae as colocalized or not by correlation with images obtained by super-resolution light microscopy (e.g. Sigal et al., 2015). Whereas ultrastructural imaging with electron microscopy can prove synaptic localization, it seems unrealistic that such methods can be used to image complete AII amacrine cells immunolabeled for synaptic proteins.

Irrespective of the problems related to light microscopic imaging of fluorescent cells and immunolabeled synaptic proteins, our analysis indicated a consistent pattern of colocalization between GluA4 and processes of AII amacrine cells when we increased the criterion for overlap from >0% to ≥50%. This was also the case when the analysis was performed separately for arboreal and lobular dendrites, suggesting that GluA4 could be involved in mediating input from both rod bipolar cells (at the arboreal dendrites) and OFF-cone bipolar cells (at the lobular dendrites). By double labeling for GluA4 and markers for postsynaptic densities (PSD95) or presynaptic ribbons (CtBP2), we observed colocalization for both combinations at both arboreal and lobular dendrites, suggesting that the GluA4 punctae overlapping with AII amacrine cells include synaptically located receptors.

Molecular basis for functional properties of AMPA receptors of AII amacrine cells

For AII amacrine cells, the kinetics of responses evoked by ultrafast application of glutamate to outside-out patches and the kinetics of spEPSCs are very similar (Veruki et al., 2003). Comparing the kinetic properties of AMPA receptors in AII amacrines with those reported for recombinant receptors, reveals that both GluA1 and GluA4 homomeric receptors display deactivation kinetics similar to those of AII amacrines. For GluA4 receptors, both flip and flop splice variants display deactivation time constants of ~0.6 ms, but for desensitization, GluA4 flop is faster (τ_{decay} ~0.9 ms) than GluA4 flip (τ_{decay} ~3.6 ms) (Mosbacher et al., 1994). The latter value is similar to the dominant (faster) time constant of desensitization for AII AMPA receptors (~3.5 ms), suggesting that only GluA4 flip is likely to contribute substantially to AII receptors. GluA1 receptors display deactivation (τ_{decay} ~1.1 ms for both

flip and flop) and desensitization kinetics (~3.4 ms for flip and ~3.7 ms for flop; Mosbacher et al., 1994) comparable to AII receptors, but their rate of recovery from desensitization ($\tau_{recovery}$ ~147 ms; Partin et al., 1996) is considerable longer than that observed for GluA4 (~6-43 ms; Lomeli et al., 1994) and AII receptors (~13 ms). Importantly, however, $\tau_{recovery}$ for GluA4 flip (6-14ms), but not $\tau_{recovery}$ for GluA4 flop (31-43 ms), is very similar to that observed for AII amacrines. Taken together, these observations suggest that GluA4 flip subunits make a substantial contribution to AMPA receptors mediating synaptic input to these cells. This interpretation is also consistent with the sensitivity of AMPA receptors of AII amacrines to cyclothiazide (Mørkve et al, 2002; Veruki et al., 2003) which more strongly potentiates the flip than the flop receptor variants (Partin et al., 1994).

In addition to GluA4, there is evidence that AII amacrine cells also express the GluA3 subunit at ribbon synaptic inputs made by rod bipolar cells. Compared to GluA4, the evidence for GluA3 is more indirect, as it is based on immunolabeling with an antibody that binds both GluA2 and GluA3 (GluA2/3), but lack of labeling with an antibody that is selective for GluA2 (Ghosh et al., 2002; Li et al., 2002; Qin and Pourcho, 1999). Nevertheless, it is pertinent to address the question of the potential contribution of GluA3 to the functional properties of the corresponding synaptic receptors and whether GluA3 might also be involved in mediating glutamatergic input from OFF-cone bipolar cells. From physiological experiments with recombinant receptors, GluA3 flip (with glycine at the R/G site) display time constants for desensitization (τ_{decay} ~4.9 ms; Lomeli et al., 1994) and recovery from desensitization ($\tau_{recovery}$ ~15 ms; Lomeli et al., 1994) that are similar to those for receptors in AII amacrines. Both GluA3 flip (with arginine at the R/G site) and GluA3 flop seem less likely to be involved, with either too slow recovery from desensitization ($\tau_{recovery}$ ~36 ms for GluA3 flip (R); Lomeli et al., 1994) or too fast desensitization (τ_{decay} ~1.4 ms; Mosbacher et al., 1994). To our knowledge, the relevant data for deactivation kinetics for GluA3 flip (G) are unfortunately not available. Important topics for future investigations will be to determine the exact composition (GluA3 vs. GluA4 and homomeric vs. heteromeric receptors), including potential associated auxiliary proteins, of the AMPA receptors at ribbon synaptic input from both rod and OFF-cone bipolar cells, the spatial distribution and density of specific types of receptors and the functional role of their kinetic properties for signaling and

synaptic integration in AII amacrine cells.

Author contributions

E.H. performed kinetic modeling and developed software for kinetic modeling, noise analysis and image analysis. B.J.Z. developed software for and performed kinetic modeling. E.M., A.C. and S.H.M. conducted electrophysiological experiments. E.M., A.C., S.H.M., M.L.V. and E.H. analyzed electrophysiological data. E.H. and M.L.V. performed cell injections, immunocytochemical experiments and image analysis. E.H. and M.L.V. conceived and designed experiments, supervised the project and interpreted data. E.H., B.J.Z. and M.L.V. wrote the manuscript and made the figures. All authors commented on and approved the final version of the manuscript.

Compliance with ethical standards

Conflict of interest The authors declare that they have no conflict of interest.

References

Barker AJ, Koch SM, Reed J, Barres BA, Ullian EM (2008) Developmental control of synaptic receptivity. J Neurosci 28:8150–8160

Bendat JS, Piersol AG (2000). Random Data. Analysis and Measurement Procedures, 3rd edn. John Wiley & Sons, New York

Bleckert A, Parker ED, Kang Y, Pancaroglu R, Soto F, Lewis R, Craig AM, Wong ROL (2013) Spatial relationships between GABAergic and glutamatergic synapses on the dendrites of distinct types of mouse retinal ganglion cells across development. PLoS ONE 8: e69612. doi:10.1371/journal.pone.0069612

Bolte S, Cordelières FP (2006) A guided tour into subcellular colocalization analysis in light microscopy. J Microsc 224:213-232

Cais O, Sedlacek M, Horak M, Dittert I, Vyklicky V Jr (2008) Temperature dependence of NR1/NR2B NMDA receptor channels. Neuroscience 151:428-438

Castilho Á, Madsen E, Ambrósio AF, Veruki ML, Hartveit E (2015) Diabetic hyperglycemia reduces Ca^{2+} permeability of extrasynaptic AMPA receptors in AII amacrine cells. J Neurophysiol 114:1545-1553

Cavelier P, Hamann M, Rossi D, Mobbs P, Attwell D (2005) Tonic excitation and inhibition of neurons: ambient transmitter sources and computational consequences. Prog Biophys Mol Biol 87:3-16

Chun MH, Han SH, Chung JW, Wässle H (1993) Electron microscopic analysis of the rod pathway of the rat retina. J Comp Neurol 332:421–432

Clements JD, Lester RAJ, Tong G, Jahr CE , Westbrook GL (1992) The time course of glutamate in the synaptic cleft. Science 258:1498-1501

Clements JD (1996) Transmitter timecourse in the synaptic cleft: its role in central synaptic function. Trends Neurosci 19:163-171

Coggan JS, Bartol TM, Esquenazi E, Stiles JR, Lamont S, Martone ME, Berg DK, Ellisman MH, Sejnowski TJ (2005) Evidence for ectopic neurotransmission at a neuronal synapse. Science 309:446-451

Colquhoun D and Hawkes AG (1995) The principles of the stochastic interpretation of ion-channel mechanisms. In: Sakmann B, Neher E (eds) Single-Channel Recording, 2nd edn. Plenum, New York, pp 397-482

Colquhoun D, Jonas P, Sakmann B (1992) Action of brief pulses of glutamate on AMPA/kainate receptors in patches from different neurones of rat hippocampal slices. J Physiol 458:261-287

Colquhoun D, Dowsland KA, Beato M, Plested AJR (2004) How to impose microscopic reversibility in complex reaction mechanisms. Biophys J 86:3510-3518

Destexhe A, Huguenard JR (2010) Modeling voltage-dependent channels. In: De Schutter E (ed) Computational Modeling Methods for Neuroscientists. MIT Press, Cambridge, pp 107-137

DeVries SH (2000) Bipolar cells use kainate and AMPA receptors to filter visual information into separate channels. Neuron 28:847-856

DeVries SH, Li W, Saszik S (2006) Parallel processing in two transmitter microenvironments at the cone photoreceptor synapse. Neuron 50:735-748

Diamond JS, Jahr CE (1997) Transporters buffer synaptically released glutamate on a submillisecond time scale. J Neurosci 17:4672-4687

Dunn KW, Kamocka MM, McDonald JH (2011) A practical guide to evaluating colocalization in biological microscopy. Am J Physiol Cell Physiol 300:C723-C742

Efron B, Tibshirani R (1993) An Introduction to the Bootstrap. Chapman & Hall / CRC, Boca Raton

Gebhardt C, Cull-Candy SG (2006) Influence of agonist concentration on AMPA and kainate channels in CA1 pyramidal cells in rat hippocampus. J Physiol 573:371-394

Geiger JRP, Roth A, Taskin B, Jonas P (1999) Glutamate-mediated synaptic excitation of cortical interneurons. In: Jonas P, Monyer H (eds) Ionotropic Glutamate Receptors in the CNS. Handbook of Experimental Pharmacology, vol. 141. Springer Verlag, Berlin, Heidelberg, pp 363-398

Ghosh KK, Haverkamp S, Wässle H (2001) Glutamate receptors in the rod pathway of the mammalian retina. J Neurosci 21:8636-8647

Hartveit E (1996) Membrane currents evoked by ionotropic glutamate receptor agonists in rod bipolar cells in the rat retinal slice preparation. J Neurophysiol 76:401-422

Hartveit E, Veruki ML (1997) AII amacrine cells express functional NMDA receptors. NeuroReport 8:1219-1223

Hartveit E, Veruki ML (2006) Studying properties of neurotransmitter receptors by non-stationary noise analysis of spontaneous synaptic currents. J Physiol 574:751-785

Hartveit E, Veruki ML (2007) Studying properties of neurotransmitter receptors by non-stationary noise analysis of spontaneous postsynaptic currents and agonist-evoked responses in outside-out patches. Nat Prot 2:434-448

Häusser M, Roth A (1997) Dendritic and somatic glutamate receptor channels in rat cerebellar Purkinje cells. J Physiol 501:77-95

Haverkamp S, Grünert U, Wässle H (2000) The cone pedicle, a complex synapse in the retina. Neuron 27:85-95

Heidelberger R, Thoreson WB, Witkovsky P (2005) Synaptic transmission at retinal ribon synapses. Prog Ret Eye Res 24:682-720

Heintzmann R (2006) Band limit and appropriate sampling in microscopy. In: Celis JE (ed) Cell Biology. A Laboratory Handbook, Vol 3. Elsevier, Amsterdam, pp 29-36

Herman MA, Jahr CE (2007) Extracellular glutamate concentration in hippocampal slice. J Neurosci 27:9736-9741

Higley MJ, Sabatini BL (2012) Calcium signaling in dendritic spines. Cold Spring Harb Perspect Biol 4: a005686

Hille B (2001) Ion Channels of Excitable Membranes, 3rd edn. Sinauer, Sunderland

Hoon M, Sinha R, Okawa H (2017). Using fluorescent markers to estimate synaptic connectivity in situ. In: Poulopoulos A (ed) Synapse Development. Methods in Molecular Biology, vol 1538. Humana Press, New York, pp 293-320

Jonas P (1995) Fast application of agonists to isolated membrane patches. In: Sakmann B, Neher E (eds) Single-Channel Recording, 2nd edn. Plenum, New York, pp 231-243

Jonas P, Major G, Sakmann B (1993) Quantal components of unitary EPSCs at the mossy fibre synapse on CA3 pyramidal cells of rat hippocampus. J Physiol 472:615-663

Kalloniatis M, Loh CS, Acosta ML, Tomisich G, Zhu Y, Nivison-Smith L, Fletcher EL, Chua J, Sun D, Arunthavasothy N (2013) Retinal amino acid neurochemistry in health and disease. Clin Exp Optom 96:310-332

Koh D-S, Geiger JRP, Jonas P, Sakmann B (1995) Ca^{2+}-permeable AMPA and NMDA receptor channels in basket cells of rat hippocampal dentate gyrus. J Physiol 485:383-402

Kolb H, Famiglietti EV (1974) Rod and cone pathways in the inner plexiform layer of cat retina. Science 186:47-49

Koulen P, Fletcher EL, Craven SE, Bredt DS, Wässle H (1998) Immunocytochemical localization of the postsynaptic density protein PSD-95 in the mammalian retina. J Neurosci 18:10136-10149

Lagnado L, Schmitz F (2015) Ribbon synapses and visual processing in the retina. Annu Rev Vis Sci 1:235-262

Lenzi D, von Gersdorff H (2001) Structure suggests function: the case for synaptic ribbons as exocytotic nanomachines. BioEssays 23:831-840

Li W, Trexler EB, Massey SC (2002) Glutamate receptors at rod bipolar ribbon synapses in the rabbit retina. J Comp Neurol 448:230-249

Lomeli H, Mosbacher J, Melcher T, Höger T, Geiger JRP, Kuner T, Monyer H, Higuchi M, Bach A, Seeburg P (1994) Control of kinetic properties of AMPA receptor channels by nuclear RNA editing. Science 266:1709-1713

Marquardt D (1963) An algorithm for least-squares estimation of nonlinear parameters. SIAM J Appl Math 11:431-441

Massey SC, Maguire G (1995) The role of glutamate in retinal circuitry. In: Wheal H, Thomson A (eds) Excitatory Amino Acids and Synaptic Transmission, 2nd edn. Academic Press, London, pp 201-221

Maxeiner S, Luo F, Tan A, Schmitz F, Südhof TC (2016) How to make a synaptic ribbon: RIBEYE deletion abolishes ribbons in retinal synapses and disrupts neurotransmitter release. EMBO J 35:1098-1114

Mehta B, Snellman J, Chen S, Li W, Zenisek D (2013) Synaptic ribbons influence the size and frequency of miniature-like evoked postsynaptic currents. Neuron 77:516-527

Mehta B, Ke J-B, Zhang L, Baden AD, Markowitz AL, Nayak S, Briggman KL, Zenisek D, Singer JH (2014) Global Ca^{2+} signaling drives ribbon-independent synaptic transmisson at rod bipolar cell synapses. J Neurosci 34:6233-6244

Momiyama A, Silver RA, Häusser M, Notomi T, Wu Y, Shigemoto R, Cull-Candy SG (2003) The density of AMPA receptors activated by a transmitter quantum at the climbing fibre-Purkinje cell synapse in immature rats. J Physiol 549:75-92

Morgans CW, Bayley PR, Oesch NW, Ren G, Akileswaran L, Taylor WR (2005) Photoreceptor calcium channels: insight from night blindness. Visual Neurosci 22:561–568

Mosbacher J, Schoepfer R, Monyer H, Burnashev N, Seeburg P, Ruppersberg JP (1994) A molecular determinant for submillisecond desensitization in glutamate receptors. Science 266:1059-1062

Moussawi K, Riegel A, Nair S, Kalivas PW (2011) Extracellular glutamate: functional compartments operate in different concentration ranges. Front Syst Neurosci 5: 94. doi: 10.3389/fnsys.2011.00094

Mørkve SH, Veruki ML, Hartveit E (2002) Functional characteristics of non-NMDA-type ionotropic glutamate receptor channels in AII amacrine cells in rat retina. J Physiol 542:147-165

Oltedal L, Hartveit E (2010) Transient release kinetics of rod bipolar cells revealed by capacitance measurement of exocytosis from axon terminals in rat retinal slices. J Physiol 588:1469-1487

Otsu N (1979) Threshold selection method from gray-level histograms. IEEE Trans Syst Man Cybern 9:62-66

Partin KM, Patneau DK, Mayer ML (1994) Cyclothiazide differentially modulates desensitization of α-amino-3-hydroxy-5-methyl-4-isoxazolepropionic acid receptor splice variants. Mol Pharmacol 46:129-138

Partin KM, Fleck MW, Mayer ML (1996) AMPA receptor flip/flop mutants affecting deactivation, desensitization, and modulation by cyclothiazide, aniracetam, and thiocyanate. J Neurosci 16:6634-6647

Plested A (2015) Ionotropic glutamate receptors. In: Zheng J, Trudeau MC (eds) Handbook of Ion Channels. CRC Press, Boca Raton, pp 307-330

Postlethwaite M, Hennig MH, Steinert JR, Graham BP, Forsythe ID (2007) Acceleration of AMPA receptor kinetics underlies temperature-dependent changes in synaptic strength at the rat calyx of Held. J Physiol 579:69-84

Qin P, Pourcho RG (1999) AMPA-selective glutamate receptor subunits GluR2 and GluR4 in the cat retina: an immunocytochemical study. Visual Neurosci 16:1105-1114

Raman IM, Trussell LO (1995) The mechanism of α-amino-3-hydroxy-5-methyl-4-isoxazolepropionate receptor desensitization after removal of glutamate. Biophys J 68:137-146

Robert A, Howe JR (2003) How AMPA receptor desensitization depends on receptor occupancy. J Neurosci 23:847-858

Rosenmund C, Stern-Bach Y, Stevens CF (1998) The tetrameric structure of a glutamate receptor. Science 280:1596-1599

Roth A, van Rossum MCW (2010) Modeling synapses. In: De Schutter E (ed) Computational Modeling Methods for Neuroscientists. MIT Press, Cambridge, pp 139-159

Sather W, Dieudonné S, MacDonald JF, Ascher P (1992) Activation and desensitization of N-methyl-D-aspartate receptors in nucleated outside-out patches from mouse neurones. J Physiol 450:643-672

Schmitz F, Königstorfer A, Südhof TC (2000) RIBEYE, a component of synaptic ribbons: a protein's journey through evolution provides insight into synaptic ribbon function. Neuron 28:857-872

Scimemi A, Beato M (2009) Determining the neurotransmitter concentration profile at active synapses. Mol Neurobiol 40:289-306

Shepherd GM, Grillner S (eds) (2010). Handbook of Brain Microcircuits. Oxford University Press, Oxford

Sigal YM, Speer CM, Babcock HP, Zhuang X (2015) Mapping synaptic input fields of neurons with super-resolution imaging. Cell 163:493-505

Sikora MA, Gottesman J, Miller RF (2005) A computational model of the ribbon synapse. J Neurosci Meth 145:47-61

Silver RA, Colquhoun D, Cull-Candy SG, Edmonds B (1996) Deactivation and desensitization of non-NMDA receptors in patches and the time course of EPSCs in rat cerebellar granule cells. J Physiol 493:167-173

Silver RA, MacAskill AF, Farrant M (2016) Neurotransmitter-gated ion channels in dendrites. In: Stuart G, Spruston N, Häusser M (eds) Dendrites, 3rd edn. Oxford University Press, New York, pp 217-257

Singer JH, Diamond JS (2003) Sustained Ca^{2+} entry elicits transient postsynaptic currents at a retinal ribbon synapse. J Neurosci 23:10923-10933

Smart TG, Paoletti P (2012) Synaptic neurotransmitter-gated receptors. Cold Spring Harb Perspect Biol 4:a009662

Smith TC, Howe JR (2000) Concentration-dependent substate behavior of native AMPA receptors. Nat Neurosci 3:992-997

Smith TC, Wang L-Y, Howe JR (2000) Heterogeneous conductance levels of native AMPA receptors. J Neurosci 20:2073-2085

Snellman J, Zenisek D, Nawy S (2009) Switching between transient and sustained signalling at the rod bipolar-AII amacrine cell synapse of the mouse retina. J Physiol 587:2443-2455

Snellman J, Mehta B, Babai N, Bartoletti TM, Akmentin W, Francis A, Matthews G, Thoreson W, Zenisek D (2011) Acute destruction of the synaptic ribbon reveals a role for the ribbon in vesicle priming. Nat Neurosci 14:1135-1141

Sterratt D, Graham B, Gillies A, Willshaw D (2011) Principles oof Computational Modelling in Neuroscience. Cambridge University Press, Cambridge

Strettoi E, Raviola E, Dacheux RF (1992) Synaptic connections of the narrow-field, bistratified rod amacrine cell (AII) in the rabbit retina. J Comp Neurol 325:152-168

Thoreson WB, Witkovsky P (1999) Glutamate receptors and circuits in the vertebrate retina. Prog Ret Eye Res 18:765-810

Traynelis SF, Silver RA, Cull-Candy SG (1993) Estimated conductance of glutamate receptor channels activated during EPSCs at the cerebellar mossy fiber-granule cell synapse. Neuron 11:279-289

Traynelis SF, Wollmuth LP, McBain CJ, Menniti FS, Vance KM, Ogden KK, Hansen KB, Yuan H, Myers SJ, Dingledine R (2010) Glutamate receptor ion channels: structure, regulation, and function. Pharmacol Rev 62:405-496

Tsukamoto Y, Omi N (2013) Functional allocation of synaptic contacts in microcircuits from rods via rod bipolar to AII amacrine cells in the mouse retina. J Comp Neurol 521:3541-3555

Tzingounis AV, Wadiche JI (2007) Glutamate transporters: confining runaway excitation by shaping synaptic transmission. Nat Rev Neurosci 8:935-947

Veruki ML, Mørkve SH, Hartveit E (2003) Functional properties of spontaneous EPSCs and non-NMDA receptors in rod amacrine (AII) cells in the rat retina. J Physiol 549:759-774

Veruki ML, Mørkve SH, Hartveit E (2006) Activation of a presynaptic glutamate transporter regulates synaptic transmission through electrical signaling. Nat Neurosci 9:1388-1396

Wadiche J, Jahr CE (2001) Multivesicular release at climbing fiber-Purkinje cell synapses. Neuron 32:301-313

Witkovsky P, Gábriel R, Krizaj D (2008) Anatomical and neurochemical characterization of dopaminergic interplexiform processes in mouse and rat retinas. J Comp Neurol 510:158-174

Wyman J, Gill SJ (1990) Binding and Linkage. Functional Chemistry of Biological Macromolecules. University Science Books, Mill Valley

Zandt B-J, Liu JH, Veruki ML , Hartveit E (2017) AII amacrine cells: quantitative reconstruction and morphometric analysis of electrophysiologically identified cells in live rat retinal slices imaged with multi-photon excitation microscopy. Brain Struct Funct 222:151-182

Zhou Y, Tencerova B, Hartveit E, Veruki ML (2016) Functional NMDA receptors are expressed by both AII and A17 amacrine cells in the rod pathway of the mammalian retina. J Neurophysiol 115:389-403

Figure legends

Fig. 1 Concentration-response relationships of AMPA receptor-mediated currents activated by application of glutamate to outside-out patches from AII amacrine cells. **a** Morphological identification of an AII amacrine cell body (arrow) in a retinal slice imaged with infrared differential interference contrast videomicroscopy. Scale bar: 10 μm. **b** Physiological identification of an AII amacrine cell with electrophysiological "signature" observed during whole-cell recording in the rat retinal slice preparation. Notice inward action currents during escape from voltage clamp evoked by 5 mV depolarizing pulses (top trace; 5 ms duration) from the holding potential (-60 mV). **c** Currents (bottom traces) activated in an outside-out patch by long (100 ms), ultrafast application of glutamate (concentrations as indicated). Here and later, the top trace represents the idealized exchange time course. Each trace is the average of 15 - 25 responses. Here and later, unless noted otherwise, recordings from outside-out patches are from conventional outside-out patches. **d** Same responses as in c, but each trace has been normalized to its peak amplitude to better visualize decreasing rise time with increasing glutamate concentration. **e** Concentration-response relationship of the peak response of glutamate-activated currents evoked by ultrafast application of long (100 ms) pulses to outside-out patches. Here, and in subsequent figures, the glutamate-activated current at each concentration is plotted as mean ± SEM. Data points normalized to the current at 5 mM (n = 4 - 16 patches for each data point). Data points have been fitted with Eq. 3. **f** Currents (bottom traces) activated in an outside-out patch by brief (~1.2 ms), ultrafast application of glutamate (concentrations as indicated). Each trace is the average of 23 - 25 responses. **g** Concentration-response relationship of the peak response of glutamate-activated currents evoked by ultrafast application of brief (~1.2 ms) pulses to outside-out patches. Data points normalized to the current at 5 mM (n = 1 - 7 patches for each data point). Data points have been fitted with Eq. 3. **h** Concentration-response relationship of the steady-state response of glutamate-activated currents evoked by application of long (100 ms) pulses to nucleated patches. Data points normalized to the current at 1 mM (n = 2 - 5 patches for each data point). Data points have been fitted with Eq. 3

Fig. 2 Concentration dependence of kinetic parameters of AMPA receptor-mediated currents activated by glutamate currents in outside-out patches from AII amacrine cells. **a** Deactivation time constant (decay phase fitted with single-exponential function, Eq. 1) for responses evoked by brief (~1.2 ms) pulses of glutamate at five different concentrations (0.5, 1, 5, 10, 30 mM; n = 4 - 6 patches for each data point). **b** Amplitude-weighted desensitization time constant (decay phase fitted with double-exponential function, Eq. 2) for responses evoked by long (100 ms) pulses of glutamate at six different concentrations (0.1, 0.5, 1, 5, 10, 30 mM; n = 3 - 15 patches for each data point). **c** Relative amplitude contribution of the two amplitude components: A_1 for the fast component (open circles) and A_2 for the slow component (filled circles) after fitting decay phase of glutamate-evoked desensitization with double-exponential function (Eq. 2) for six different concentrations (as in b; n = 3 - 15 patches for each data point). **d** Rise time (20-80%) of responses evoked by short (~1.2 ms; S, open circles) or long (100 ms; L, filled circles) pulses of glutamate at six different concentrations (as in b; n = 3 - 15 patches for each data point). Because of unequal weighting related to variable number of patches for each data point, rise times were first normalized to that at 5 mM for each patch, averaged and multiplied again with the mean rise time at 5 mM

Fig. 3 Equilibrium desensitization of AMPA receptors in AII amacrine cells. **a** Currents (bottom traces) activated in two different outside-out patches by long (100 ms), ultrafast application of glutamate (3 mM) after pre-exposing the patches to different concentrations of glutamate (as indicated) for 1.75 s. Traces labeled "Control" evoked by glutamate without pre-exposure to glutamate. Notice how pre-exposure to increasing concentrations of glutamate reduces the peak amplitude of the response evoked by 3 mM glutamate. Top traces represent pre-exposure to glutamate (dashed line) and ultrafast application of glutamate (continuous line). Each trace is the average of 4 - 25 responses. **b** Concentration-inhibition relationship (filled circles) of the peak response of glutamate-activated (3 mM) currents evoked by ultrafast application of long (100 ms) pulses to outside-out patches pre-exposed to different concentratios of glutamate (0.3 to 100 μM; n = 3 - 11 patches for each data point). Data points normalized to the current evoked by glutamate (3 mM) without pre-exposure to glutamate such that "1" and "0" correspond to no and complete equilibrium

desensitization, respectively. Data points have been fitted with Eq. 3. For comparison, graph also shows concentration-response relationship (as in Fig. 1e; open circles; data points fitted with Eq. 3). The graphs of the two fitted curves have been scaled such that the maximum for the concentration-inhibition relationship (1; *left* Y-axis) coincides with the maximum for the concentration-response relationship (1.35; *right* Y-axis)

Fig. 4 Single-channel conductance and maximum open probability ($P_{open,\,max}$) of AMPA receptors in AII amacrine cells obtained by non-stationary noise analysis of glutamate-evoked responses in an outside-out patch from an AII amacrine cell. **a** Three individual responses (*black* traces) obtained by brief (~1.2 ms) pulses of glutamate (3 mM), the ensemble mean waveform (*red* trace) has been superimposed on each trace. Horizontal scale bar (5 ms) also applies to traces in b - d. **b** three difference currents calculated from corresponding individual records (displayed in a) and mean waveform (*red* trace in a). **c** Ensemble mean of all glutamate-evoked responses (n = 20 repetitions). Broken horizontal lines indicate amplitude intervals used for binning mean current and variance such that each bin on average corresponds to a constant number of channel closures. **d** Ensemble current variance (without binning) of all glutamate-evoked responses, calculated from the differences between individual records and the ensemble mean waveform (as in b). **e** Ensemble current variance (from d) *versus* mean current (after binning, from c; bottom axis) and open probability (P_{open}; top axis). Time range used for the variance *versus* mean graph corresponds to the data points from the peak of the mean waveform to the end of the decay phase. Data points were fitted with Eq. 4

Fig. 5 Kinetic scheme and model responses (AII-HR97) for AMPA receptors in AII amacrine cells. **a** Kinetic scheme of a model proposed for AMPA receptor gating in AII amacrine cells (original scheme with different rate constants proposed for gating of AMPA receptors in cerebellar Purkinje cells; Häusser and Roth, 1997). C0: unbound state; C1: singly liganded state; C2: doubly liganded state; O: open state; C3: singly liganded, desensitized state; C4, C5, C6 and C7: doubly liganded, desensitized states. A rate constant labelled k_{AB} indicates the transition rate from state A to state B. Here and later, when a rate constant has the unit of M^{-1}

in addition to s^{-1}, it indicates a ligand-binding step. The rate constants were as follows: k_{C0C1} = 19.7 × 10^6 M^{-1} s^{-1}, k_{C1C0} = 845 s^{-1}, k_{C1C2} = 2.16 × 10^6 M^{-1} s^{-1}, k_{C2C1} = 20.8 × 10^3 s^{-1}, k_{C2O} = 117 × 10^3 s^{-1}, k_{OC2} = 5.87 × 10^3 s^{-1}, k_{OC7} = 148 s^{-1}, k_{C7O} = 68.6 s^{-1}, k_{C1C3} = 708 s^{-1}, k_{C3C1} = 161 s^{-1}, k_{C2C4} = 184 s^{-1}, k_{C4C2} = 3.29 s^{-1}, k_{OC5} = 82.3 × 10^{-3} s^{-1}, k_{C5O} = 50.3 × 10^{-3} s^{-1}, k_{C7C6} = 57.9 s^{-1}, k_{C6C7} = 4.06 s^{-1}, k_{C3C4} = 6.99 × 10^6 M^{-1} s^{-1}, k_{C4C3} = 5.30 × 10^3 s^{-1}, k_{C4C5} = 53.7 s^{-1}, k_{C5C4} = 92.0 s^{-1}, k_{C5C6} = 4.62 × 10^3 s^{-1}, k_{C6C5} = 246 s^{-1}. **b** Macroscopically simulated responses evoked by brief pulses (1 ms; *left*) or steps (*middle*) of glutamate (0.3, 1, 3, 10 and 30 mM) and to variable duration (1, 5, 10, 20, 30 and 100 ms; *right*) pulses of glutamate (3 mM). Time course of glutamate application indicated above response traces. **c** Macroscopically simulated response (*bottom*) evoked by a glutamate concentration profile (*top*) designed to mimick a synaptic concentration profile generated by release of a single transmitter vesicle (instantaneous rise followed by double-exponential decay with parameters τ_1 = 0.1 ms, A_1 = 3 mM, τ_2 = 1 ms, A_2 = 0.5 mM). **d** Macroscopically simulated response (*bottom*) evoked by a glutamate concentration profile (*top*) designed to mimick a synaptic concentration profile generated by release of 10 transmitter vesicles at a frequency of 5 kHz (with temporal summation of individual concentration profiles as in c)

Fig. 6 Kinetic scheme and model responses (AII-RH03) for AMPA receptors in AII amacrine cells. **a** Kinetic scheme of a model proposed for AMPA receptor gating in AII amacrine cells (original scheme with different rate constants proposed for gating of recombinant, homomeric AMPA receptors composed of GluA4 subunits; Robert and Howe, 2003). R0: unbound state; R1: singly liganded, closed state; R2: doubly liganded, closed state; R3: triply liganded, closed state; R4: quadruply liganded, closed state; O2: doubly liganded, open state; O3: triply liganded, open state; O4: quadruply liganded, open state; D0-D4 and $D_2$2-$D_2$4: desensitized, closed states, liganded as indicated. The rate constants were as follows: α = 808 × 10^3 s^{-1}, β = 2.34 × 10^6 s^{-1}, k_1 = 9.77 × 10^6 M^{-1} s^{-1}, k_{-1} = 4.13 × 10^3 s^{-1}, k_{-2} = 3.05 × 10^{-6} s^{-1}, δ_0 = 1.64 × 10^{-9} s^{-1}, γ_0 = 0.631 s^{-1}, δ_1 = 806 s^{-1}, γ_1 = 76.4 s^{-1}, δ_2 = 19.8 s^{-1}, γ_2 = 6.71 s^{-1}. The relative single-channel conductances were as follows: γ_{O2} = 0.333, γ_{O3} = 0.667, γ_{O4} = 1. **b** Macroscopically simulated responses evoked by brief pulses (1 ms; *left*) or steps (*middle*) of glutamate (0.3, 1, 3, 10 and 30 mM) and to variable duration (1, 5, 10, 20, 30 and 100 ms; *right*) pulses of glutamate (3 mM). Time course of glutamate application indicated above response traces. **c**

Macroscopically simulated response (*bottom*) evoked by a glutamate concentration profile (*top*) designed to mimick a synaptic concentration profile generated by release of a single transmitter vesicle (instantaneous rise followed by double-exponential decay with parameters τ_1 = 0.1 ms, A_1 = 3 mM, τ_2 = 1 ms, A_2 = 0.5 mM). **d** Macroscopically simulated response (*bottom*) evoked by a glutamate concentration profile (*top*) designed to mimick a synaptic concentration profile generated by release of 10 transmitter vesicles at a frequency of 5 kHz (with temporal summation of individual concentration profiles as in c)

Fig. 7 Determining the apparent $P_{open,\,max}$ for the AII-RH03 kinetic model with multiple open states and multiple conductance levels. **a** Macroscopically simulated state occupancies for the doubly, triply and quadruply liganded open states O2, O3 , and O4 (see kinetic scheme in Fig. 6a) evoked by a brief pulse of glutamate (1.2 ms, 3 mM; *top* trace). **b** Macroscopically simulated current response for the same stimulus as in a. The relative conductances for states O2, O3, and O4 were set to 0.333, 0.667 and 1, respectively. The rate constants were set to the values stated in Fig. 6. The current generated by a fully populated state O4 was normalized to 1. ***C***, Variance of the current response in b. The part from just before the peak to the end of the response (marked by the thicker line) was used for the determination of $P_{open,\,max}$. **d** Plot of variance (as in c) *versus* mean current (as in b) after resampling at evenly spaced points (open circles). Data points were fitted with Eq. 4 (continuous line)

Fig. 8 Non-stationary noise analysis of responses generated by the AII-HR97 (a - d) and AII-RH03 (e - h) kinetic schemes for AMPA receptors in AII amacrine cells. **a** Variance *versus* mean curves for stochastically simulated responses after conventional non-stationary noise analysis of responses evoked by square-wave pulses of glutamate (1 ms duration) at five glutamate concentrations (0.3, 1, 3, 5, and 100 mM) for the AII-HR97 kinetic scheme. N (number of available channels) = 50, single-channel conductance (γ) = 24.5 pS, driving force = -60 mV, single-channel current = 1.47 pA, n (number of repetitions) = 1000. Here and below, continuous lines represent results for the different glutamate concentrations and the broken line represents the theoretical curve calculated according to Eq. 4. **b** Variance *versus* mean curves for stochastically simulated responses with trial-to-trial variation (Gaussian) in

the number of available channels (N = 50 ± 10 (SD); n = 1000) after conventional non-stationary noise analysis. **c** Variance *versus* mean curves for stochastically simulated responses (N = 50; n = 1000) after peak-scaled (PS) non-stationary noise analysis. **d** Variance *versus* mean curves for stochastically simulated responses with trial-to-trial variation (Gaussian) in the number of available channels (N = 50 ± 10; n = 1000) after peak-scaled non-stationary noise analysis. **e** Variance *versus* mean curves for stochastically simulated responses after conventional non-stationary noise analysis of responses evoked by square-wave pulses of glutamate (1 ms duration) at five glutamate concentrations (0.3, 1, 3, 5, and 100 mM) for the AII-RH03 kinetic scheme. N = 50, single-channel conductances (γ) = 12 (O2), 24 (O3) and 36 (O4) pS, driving force = -60 mV, single-channel currents = 0.72 (O2), 1.44 (O3) and 2.16 (O4) pA, n = 1000. **f - h**, as in b - d, but for the AII-RH03 kinetic scheme

Fig. 9 Covariance functions for responses to brief pulses of glutamate generated by two different kinetic schemes (AII-HR97 and AII-RH03) for AMPA receptors of AII amacrine cells. **a** Ensemble mean response generated by AII-HR97 kinetic scheme (*bottom* trace). Here and in d, 1 ms glutamate pulses (3 mM) with 20-80% rise and decay time 0.25 ms (*top* traces). N (number of available channels) = 50, single-channel conductance (γ) = 24.5 pS, driving force = 60 mV, single-channel current = 1.47 pA, n (number of repetitions) = 1000. Here, and in d and g, the decay time constant (τ_{decay}) indicated in panel. **b** Two-dimensional covariance function for responses generated by AII-HR97 kinetic scheme (a), variance coded according to color bar to the right of panel, diagonal (top left to bottom right) corresponds to ensemble variance (c). Here, and in e and h, scaling of top axis is identical to X-axis scaling of a, d, and g, respectively. **c** Variance (*black* continuous trace) for AII-HR97 response ensemble and covariance function (*red* trace) with center point (t_c) corresponding to location of peak response of ensemble mean waveform. Single-exponential fit (broken line) overlaid on covariance function, decay time constant (τ_{decay}) indicated in panel. **d** Ensemble mean response generated by kinetic scheme AII-RH03 with multiple open states and conductance levels. N = 50, single-channel conductances (γ) = 12 (O2), 24 (O3) and 36 (O4) pS, driving force = 60 mV, single-channel currents = 0.72 (O2), 1.44 (O3) and 2.16 (O4) pA, n = 1000. **e** Two-dimensional covariance function for responses generated by AII-RH03 kinetic scheme

(d), variance coded according to color bar to the right of panel h, diagonal (top left to bottom right) corresponds to ensemble variance (f). **f** Variance (*black* continuous trace) for AII-RH03 response ensemble and covariance function (*red* trace) with center point (t_c) corresponding to location of peak response of ensemble mean waveform. Single-exponential fit (broken line) overlaid on covariance function, decay time constant (τ_{decay}) indicated in panel. **g** Ensemble mean response (n = 52 repetitions) activated in an outside-out patch from an AII amacrine cell by brief (~1.2 ms), ultrafast application of glutamate (3 mM). Small notch during decay phase represents a brief oscillation of glutamate application. **h** Two-dimensional covariance function for responses activated in outside-out patch (g), variance coded according to color bar to the right, diagonal (top left to bottom right) corresponds to ensemble variance (i). Small "lobes" occurring at ~22 ms correspond to response oscillation in g. **i** Variance (*black* continuous trace) for outside-out response ensemble and covariance function (*red* trace) with center point (t_c) corresponding to location of peak response of ensemble mean waveform. Single-exponential fit (broken line) overlaid on covariance function, decay time constant (τ_{decay}) indicated in panel. When fitting the decays in g and i with single-exponential functions, the period corresponding to the brief oscillation was ignored during the fit

Fig. 10 Colocalization between AII amacrine cells and immunolabeled punctae of the AMPA receptor subunit GluA4. **a** Maximum intensity projection of confocal image stack of retinal slice with an AII amacrine cell injected with Alexa Fluor 488 (*green*) and immunolabeled for GluA4 (*magenta*). Here and later, all images and graphs were generated from digital data after deconvolution (for details, see Materials and methods). Cell appears compressed along the vertical axis due to distortion around apical dendrite during tissue processing. Here and later, arrow head (*right*) marks division between sublamina *a* (*above*) and sublamina *b* (*below*) of inner plexiform layer with lobular and arboreal processes of AII amacrine, respectively. All images and graphs (b - n) from same cell as in a. Scale bar, 5 μm. **b** Examples of colocalization (arrow heads) of GluA4 punctate (*magenta*) with AII amacrine lobular processes (*green*) in sublamina *a*. Here and in c, each image taken from a single confocal slice. Scale bar, 2 μm. **c** Examples of colocalization (arrow heads) of GluA4 punctate (*magenta*) with AII amacrine arboreal processes (*green*) in sublamina *b*. Scale bar, 2 μm. **d**

Three-dimensional (3D) surface rendering of AII amacrine cell and locations of immunolabeled GluA4 punctae overlapping with the AII amacrine (after threshold-based segmentation). Each punctum is visualized by a sphere of arbitrary size with center located at the intensity-weighted 3D (XYZ) center-of-mass coordinates of the punctum. GluA4 punctae with overlap between 0 and 50% displayed as smaller *yellow* spheres and punctae with ≥50% overlap displayed as larger *magenta* spheres. **e** Frequency histogram of distance from center-of-mass coordinates of thresholded GluA4 punctae overlapping with AII amacrine cell (d) to nearest point on surface of segmented AII amacrine cell. Bin width 0.1 μm. **f** Frequency histogram of relative colocalization between segmented GluA4 punctae (that overlapped with the segmented AII amacrine cell) and the AII amacrine cell. Bin width 10%. **g** Scatter plot with data in e and f of relationship between distance from GluA4 punctae (center of mass) to AII amacrine surface and relative colozalization between GluA4 punctae and AII amacrine. **h** Average signal in GluA4 channel around 3D coordinates (XYZ; center of mass, CM) of thresholded GluA4 punctae (overlapping with AII amacrine cell), displayed as 2D image (*top*) through center of extracted volume of average signal (in XY plane) and linear intensity profile (*bottom*; measured in arbitrary units, a.u.) across center of displayed 2D image. Here and later, spatial scale of line profile also applies to corresponding 2D image. 2D images in h - n displayed with same intensity range. **i** Average signal in AII amacrine channel around 3D coordinates of all thresholded GluA4 punctae overlapping with AII amacrine cell, displayed as 2D image (*top*) through center of extracted volume of average signal and linear intensity profile (*bottom*) across center of displayed 2D image. **j** As in i, but only for GluA4 punctae located at AII amacrine lobular processes in sublamina *a*. **k** As in i, but only for GluA4 punctae located at AII amacrine arboreal processes in sublamina *b*. **l - n** As for i - k, but only for GluA4 punctae with ≥50% overlap with AII amacrine cell

Fig. 11 Number of immunolabeled GluA4 punctae overlapping AII amacrine cells as a function of relative overlap between the segmented GluA4 punctae and each cell (from >0% to 100%, increments of 10%). Relative overlap for a given GluA4 punctum measured as the fraction of the total volume of the segmented punctum occupied by an object belonging to the segmented AII amacrine cell. Data points for individual AII amacrine cells (n = 8) are

represented by gray circles and data points for the same cell are connected by lines. Black circles (connected by lines) represent mean ± SEM for each value of overlap

Fig. 12 Colocalization between AII amacrine cells, immunolabeled punctae of the AMPA receptor subunit GluA4 and immunolabeled punctae of the postsynaptic scaffold protein PSD95. **a** Maximum intensity projection of confocal image stack of retinal slice with an AII amacrine cell injected with Alexa Fluor 488 (*green*) and immunolabeled for GluA4 (*magenta*) and PSD95 (*blue*). All images and graphs (b - i) from same cell as in a. Scale bar, 5 μm. **b** Examples of colocalization (arrow heads) of GluA4 punctae (*magenta*; displayed separately in b2) and PSD95 punctae (*blue*; displayed separately in b3) with AII amacrine lobular processes (*green*; overlaid with GluA4 and PSD95 signals in b1) located in sublamina *a*. Here and in c, each image taken from a single confocal slice. Scale bar, 1 μm. **c** Examples of colocalization (arrow heads) of GluA4 punctae (*magenta*; displayed separately in c2) and PSD95 punctae (*blue*; displayed separately in c3) with AII amacrine arboreal processes (*green*; displayed with GluA4 and PSD95 signals overlaid in c1) located in sublamina *b*. Scale bar, 1 μm. **d** Average signal in PSD95 channel around 3D coordinates (XYZ; center of mass, CM) of all thresholded GluA4 punctae (overlapping with AII amacrine cell), displayed as 2D image (*top*) through center of extracted volume of average signal (in XY plane) and linear intensity profile (*bottom*) across center of displayed 2D image. 2D images in d - i displayed with same intensity range. **e** As in d, but only for GluA4 punctae located at AII amacrine lobular processes in sublamina *a*. **f** As in d, but only for GluA4 punctae located at AII amacrine arboreal processes in sublamina *b*. **g - i** As for d - f, but only for GluA4 punctae with ≥50% overlap with AII amacrine cell

Fig. 13 Colocalization between AII amacrine cells, immunolabeled punctae of the AMPA receptor subunit GluA4 and immunolabeled punctae of the presynaptic ribbon protein CtBP2. **a** Maximum intensity projection of confocal image stack of retinal slice with an AII amacrine cell injected with Alexa Fluor 488 (*green*) and immunolabeled for GluA4 (*magenta*) and CtBP2 (*blue*). All images and graphs (b - i) from same cell as in a. Scale bar, 7.5 μm. **b** Examples of colocalization (arrow heads) of GluA4 punctae (*magenta*; displayed separately in

b2) and CtBP2 punctae (*blue*; displayed separately in b3) with AII amacrine lobular processes (*green*; overlaid with GluA4 and CtBP2 signals in b1) located in sublamina *a*. Here and in c, each image taken from a single confocal slice. Scale bar, 1 μm. **c** Examples of colocalization (arrow heads) of GluA4 punctae (*magenta*; displayed separately in c2) and PSD95 punctae (*blue*; displayed separately in c3) with AII amacrine arboreal processes (*green*; overlaid with GluA4 and CtBP2 signals in c1) located in sublamina *b*. Scale bar, 1 μm. **d** Average signal in CtBP2 channel around 3D coordinates (XYZ; center of mass; CM) of all thresholded GluA4 punctae (overlapping with AII amacrine cell), displayed as 2D image (*top*) through center of extracted volume of average signal (in XY plane) and linear intensity profile (*bottom*) across center of displayed 2D image. 2D images in d - i displayed with same intensity range. **e** As in d, but only for GluA4 punctae located at AII amacrine lobular processes in sublamina *a*. **f** As in d, but only for GluA4 punctae located at AII amacrine arboreal processes in sublamina *b*. **g - i** As for d - f, but only for GluA4 punctae with ≥50% overlap with AII amacrine cell

Table 1. Primary antibodies

Antibody name	Immunogen	Source, cat #, RRID	Antibody type	Dilution
GluA4	C-terminus of GluA4 receptor	Millipore AB-1508, AB_90711	Rabbit, polyclonal	1:1600
PSD95	Clone 6G6-1C9, purified recombinant rat PSD-95	ThermoFisher Scientific MA1-045, AB_325399	Mouse, monoclonal	1:3200
CtBP2	Mouse CtBP2 aa. 361-445	BD Biosciences Cat# 612044 AB_399431	Mouse, monoclonal	1:1000

RRID is Resource Identification Portal: https://scicrunch.org/resources

The table summarizes antibodies used in the present study. The specificity of the rabbit antiserum against the AMPA receptor subunit GluA4 was demonstrated by the manufacturer. The antibody detects a single band of ~100 kDa in western blots of rat brain lysate. The same antibody has been used in a number of studies carried out in the mammalian retina, including Haverkamp et al. (2000), Witkovsky et al. (2008) and Kalloniatis et al. (2013). The specificity of the mouse monoclonal antibody against purified recombinant rat PSD95 was demonstrated by the manufacturer. This antibody has been used in the retina in numerous studies including Koulen et al. (1998), Barker et al. (2009) and Bleckert et al. (2013). The specificity of the mouse antibody against the C-terminal Binding Protein-2 (CtBP2) has been characterized by the manufacturer. It detects a single band of ~48 kDa in western blots of BC3H1 cell lysate (mouse brain smooth muscle-like cells; ATCC CRL-1443). The antibody has been used in several studies in the retina to detect synaptic ribbons, including Morgans et al. (2005) and Maxeiner et al. (2016).

Table 2. Experimental observables for ionotropic non-NMDA (AMPA) type glutamate receptors of AII amacrine cells in rat retina

Observable	Experiment (Mean ± SEM/SE)	Used for fitting	Model AII-HR97	Model AII-RH03
20-80% rise time (ms), [Glu] = 3 mM[a]	0.274 ± 0.024	x	0.279	0.328
Deactivation τ (ms), [Glu] = 3 mM[a]	1.07 ± 0.12	x	1.08	1.12
Desensitization τ_1 (ms), [Glu] = 3 mM[a]	3.52 ± 0.46	x	3.58	2.95
Desens. τ_1 (ms), [Glu] = 3 mM, rel. contribution (%)[a]	74.0 ± 5.9	x	73.4	70.3
Desensitization τ_2 (ms), [Glu] = 3 mM[a]	20.8 ± 3.9	x	21.0	22.4
Desens. τ_2 (ms), [Glu] = 3 mM, rel. contribution (%)[a]	26.0 ± 5.9		26.6	29.7
Non-desensitizing current (%), [Glu] = 3 mM[a]	4.23 ± 0.95	x	4.24	4.50
Recovery τ from brief pulse desensitization (ms), [Glu] = 3 mM[b]	13.3 ± 1.9	x	14.1	16.2
Recovery invTau from brief pulse desensitization (ms^{-1}), [Glu] = 3 mM[b]	0.075 ± 0.011		0.071	0.062
Maximal depression of second pulse after brief pulse desensitization (%)[c]	61.8 ± 5.2	x	61.0	53.8
$P_{o,\,max}$ [Glu] = 3 mM	0.613 ± 0.020	x	0.602	0.468
Single-channel conductance (γ) from non-stationary noise analysis of outside-out patches (pS), [Glu] = 3 mM	24.5 ± 2.7			
Peak concentration-response EC_{50} (mM)	1.53		1.05	0.82
Peak concentration-response $\log_{10}(EC_{50})$	-2.82 ± 0.11	x	-2.98	-3.09
Peak concentration-response Hill coefficient	0.99 ± 0.17	x	1.07	0.85
Steady-state concentration-response EC_{50} (μM)	693		77	56
Steady-state concentration-response $\log_{10}(EC_{50})$	-3.16 ± 0.39		-4.11	-4.25
Steady-state concentration-response Hill coefficient	0.55 ± 0.18		1.14	1.16
Equilibrium desensitization IC_{50} (μM)	10.5		11.3	10.0
Equilibrium desensitization $\log_{10}(IC_{50})$	-4.98 ± 0.12	x	-4.95	-5.00
Equilibrium desensitization Hill coefficient	0.84 ± 0.17	x	0.87	0.94

[a] From Veruki et al. (2003)
[b] Reanalyzed from Veruki et al. (2003). The SE of the recovery τ was calculated from the SE of the inverse time constant (invTau) such that the relative SEs of τ and invTau were the same.
[c] Reanalyzed from Veruki et al. (2003).

Table 3. AII-HR97

A

		300 μM	1 mM	3 mM	5 mM	100 mM
	Parabolic fit:					
i	mean ± SEM (pA)	1.50 ± 0.025	1.44 ± 0.051	1.43 ± 0.024	1.43 ± 0.023	1.49 ± 0.011
	CV	0.052 (0.068)	0.112 (0.066)	0.053 (0.049)	0.051 (0.045)	0.023 (0.049)
	Bias (%)	1.9	-1.8	-2.5	-2.7	1.2
N	mean ± SEM	48.5 ± 6.0	56.3 ± 5.2	52.8 ± 1.2	51.7 ± 1.0	49.2 ± 0.4
	CV	0.391 (3.505)	0.291 (0.174)	0.074 (0.081)	0.062 (0.064)	0.022 (0.052)
	Bias (%)	-3.0	12.6	5.6	3.4	-1.5

B

		300 μM	1 mM	3 mM	5 mM	100 mM
Linear fit:						
i	mean ± SEM (pA)	1.50 ± 0.013	1.50 ± 0.019	1.53 ± 0.016	1.56 ± 0.021	1.57 ± 0.022
	CV	0.028 (0.041)	0.039 (0.044)	0.033 (0.043)	0.043 (0.046)	0.043 (0.044)
	Bias (%)	1.8	1.8	4.2	6.2	6.5
Parabolic fit (after peak-scaling):						
i	mean ± SEM (pA)	1.50 ± 0.030	1.42 ± 0.023	1.46 ± 0.030	1.50 ± 0.031	1.46 ± 0.021
	CV	0.063 (0.046)	0.050 (0.050)	0.066 (0.044)	0.065 (0.056)	0.045 (0.042)
	Bias (%)	1.9	-3.2	-0.91	1.8	-0.83
N	mean ± SEM	9.03 ± 0.20	28.7 ± 1.3	53.5 ± 1.9	51.0 ± 1.3	53.0 ± 1.0
	CV	0.071 (0.058)	0.139 (0.096)	0.114 (0.077)	0.080 (0.077)	0.058 (0.049)

A, AII-HR97, simulations (1 ms square-wave agonist pulses with concentration as indicated) with constant number of channels (γ = 24.5 pS; i = 1.47 pA; N = 50; n = 1000). Here and later, i (unitary current) and N (number of channels) calculated with

conventional non-stationary noise analysis, curve fit with parabolic function (Eq. 4). Here and later, CV calculated from analysis of 10 repetitions, CV in parentheses obtained from bootstrap re-sampling of 100 synthetic data sets from one of the original data sets.

B, AII-HR97, simulations with stochastic trial-to-trial variation of the number of channels (γ = 24.5 pS; i = 1.47 pA; N = 50; SD = 10; n = 1000). Here and later, upper row (i) indicates results from non-stationary noise analysis with no peak-scaling and linear fit to initial part of the variance *versus* mean curve, lower two rows (i and N) indicate results from peak-scaled non-stationary noise analysis and parabolic fit (Eq. 4).

Table 4. AII-RH03

A

		300 μM	1 mM	3 mM	5 mM	100 mM
	Parabolic fit:					
i	mean ± SEM (pA)	1.01 ± 0.053	1.21 ± 0.017	1.29 ± 0.016	1.31 ± 0.016	1.46 ± 0.016
	CV	0.053 (0.044)	0.043 (0.045)	0.040 (0.048)	0.039 (0.044)	0.035 (0.035)
N	mean ± SEM	67.5 ± 3.2	86.7 ± 2.9	100.5 ± 2.2	101.2 ± 2.3	84.1 ± 1.0
	CV	0.150 (0.120)	0.104 (0.090)	0.070 (0.088)	0.073 (0.087)	0.037 (0.048)

B

		300 μM	1 mM	3 mM	5 mM	100 mM
Linear fit:						
i	mean ± SEM (pA)	1.02 ± 0.013	1.28 ± 0.018	1.36 ± 0.016	1.46 ± 0.019	1.47 ± 0.026
	CV	0.040 (0.042)	0.043 (0.043)	0.038 (0.039)	0.040 (0.037)	0.056 (0.037)
Parabolic fit (after peak-scaling):						
i	mean ± SEM (pA)	0.91 ± 0.009	1.07 ± 0.013	1.25 ± 0.026	1.28 ± 0.022	1.38 ± 0.020
	CV	0.031 (0.052)	0.038 (0.057)	0.066 (0.048)	0.053 (0.041)	0.046 (0.040)
N	mean ± SEM	48.5 ± 2.1	80.8 ± 2.6	112.1 ± 6.3	119.0 ± 4.4	109.2 ± 3.1
	CV	0.140 (0.135)	0.103 (0.143)	0.178 (0.112)	0.117 (0.097)	0.089 (0.076)

A, AII-RH03, simulations (1 ms square-wave agonist pulses with concentration as indicated) with constant number of channels (γ = 12, 24 and 36 pS; i = 0.72, 1.44 and 2.16 pA; N = 50; n = 1000).

B, AII-RH03, simulations with stochastic trial-to-trial variation of the number of channels (γ = 12, 24 and 36 pS; i = 0.72, 1.44 and 2.16 pA; N = 50; SD = 10; n = 1000).

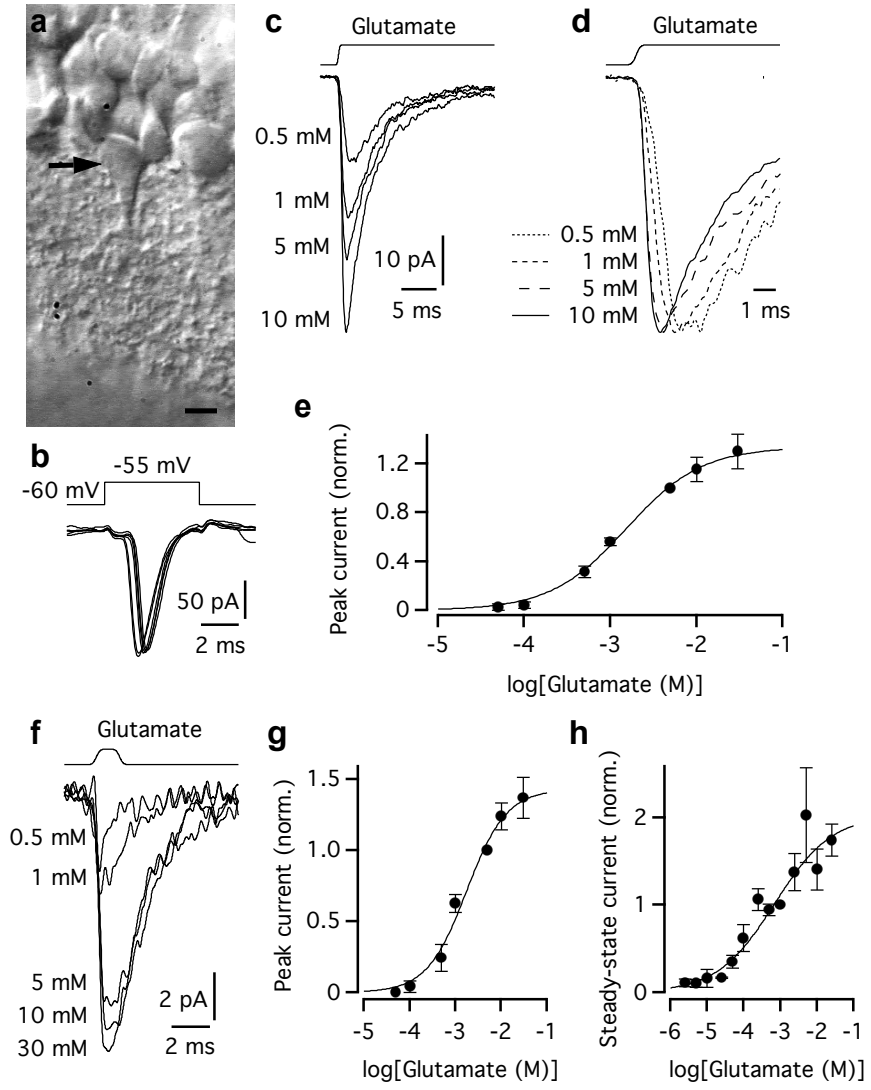

Fig. 1 (Hartveit et al., 2017)

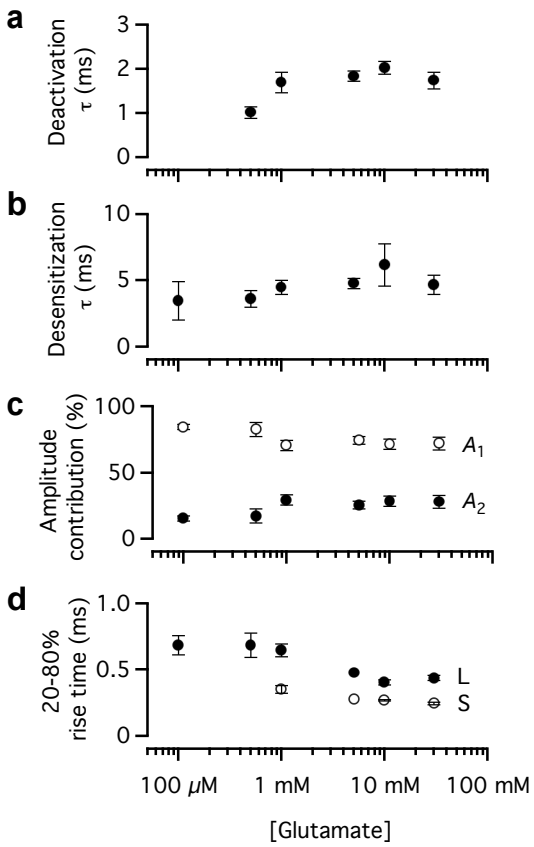

Fig. 2 (Hartveit et al., 2017)

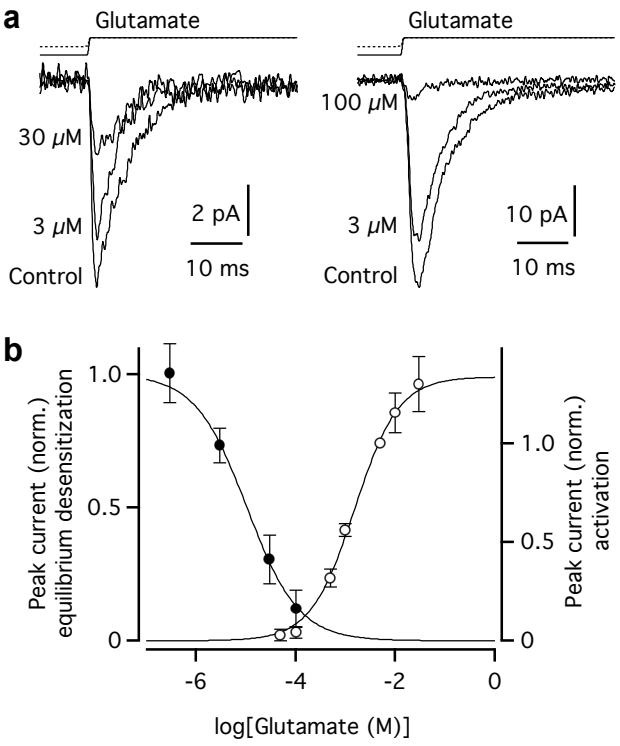

Fig. 3 (Hartveit et al., 2017)

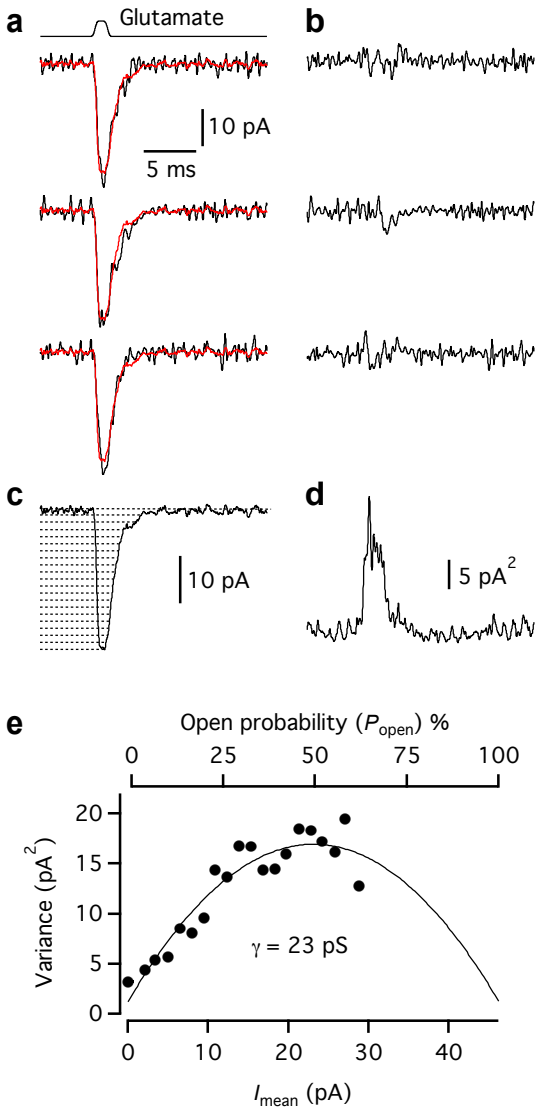

Fig. 4 (Hartveit et al., 2017)

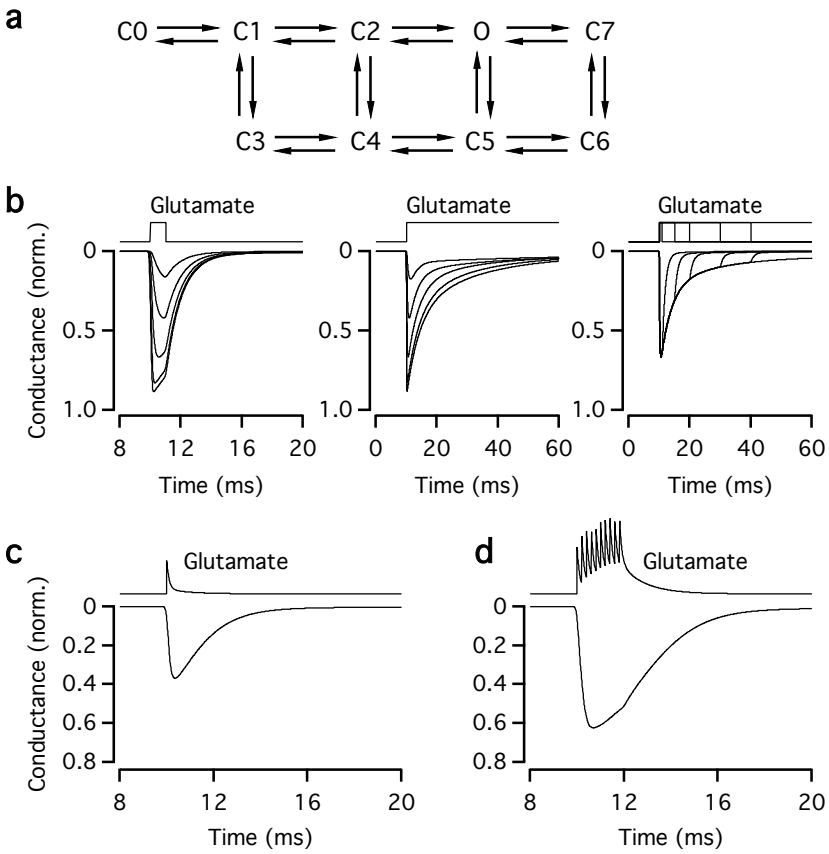

Fig. 5 (Hartveit et al., 2017)

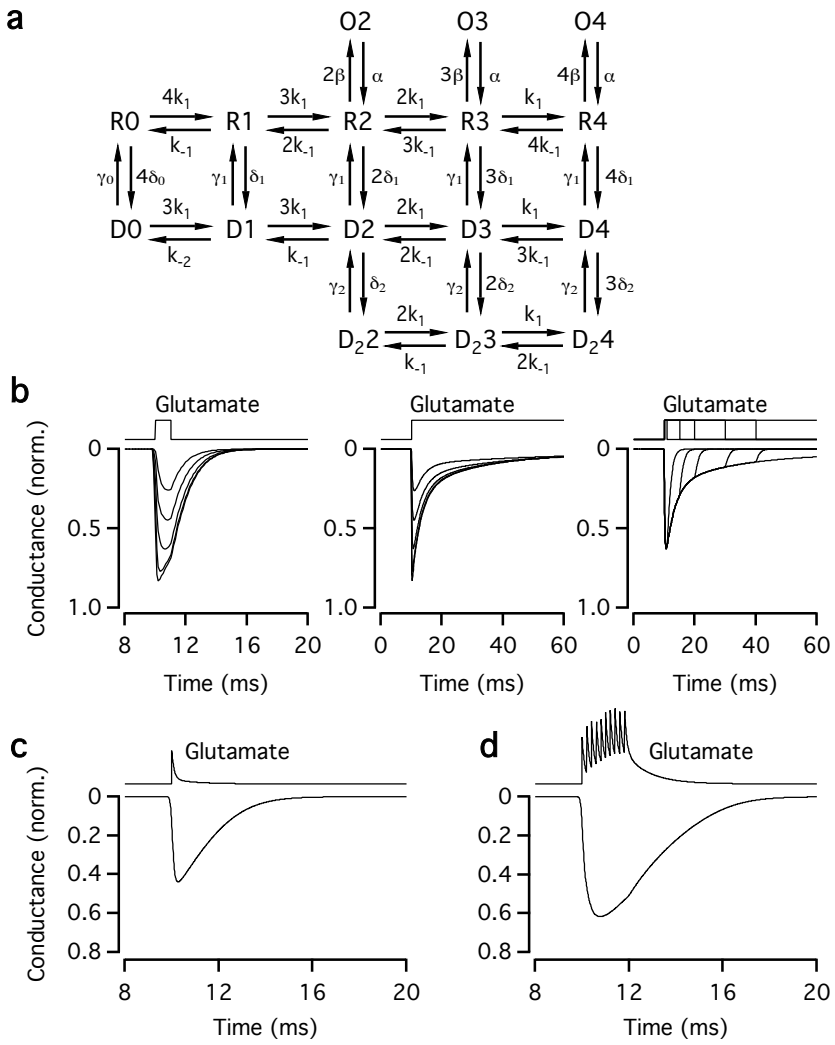

Fig. 6 (Hartveit et al., 2017)

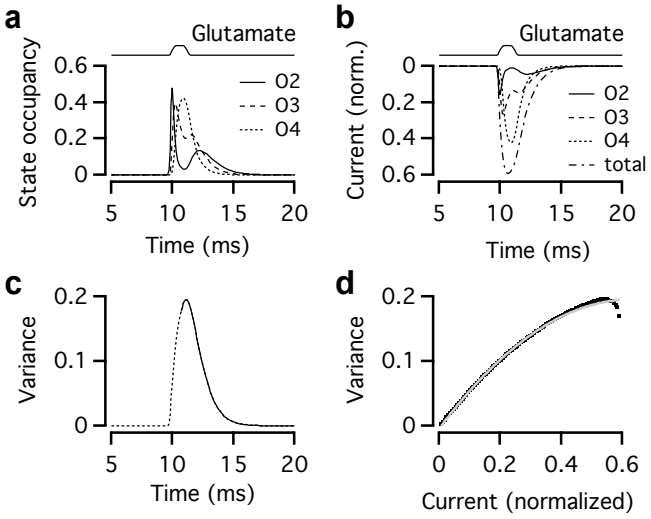

Fig. 7 (Hartveit et al., 2017)

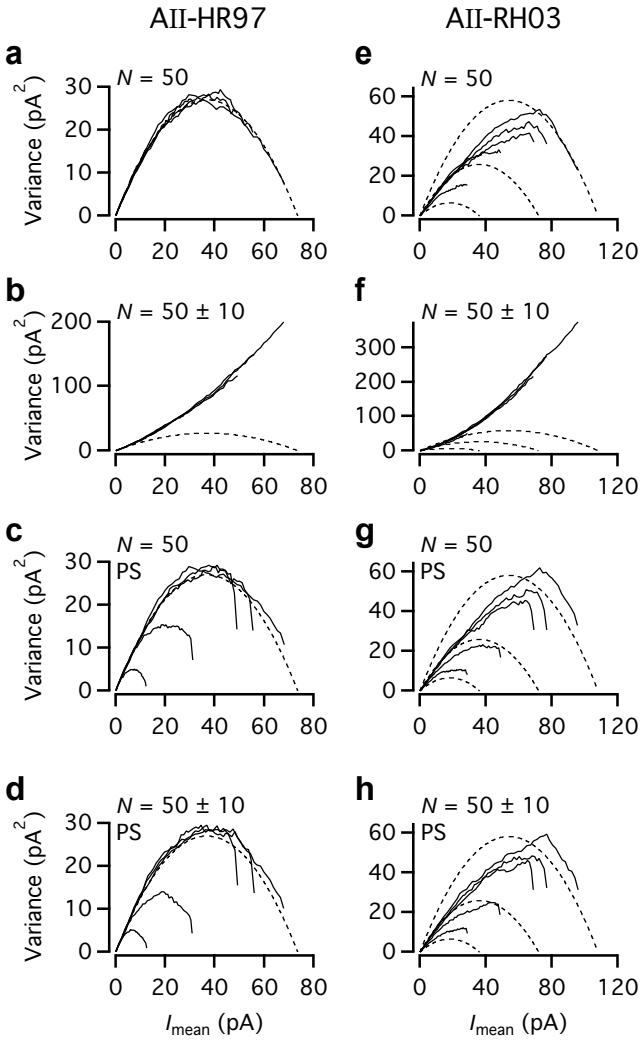

Fig. 8 (Hartveit et al., 2017)

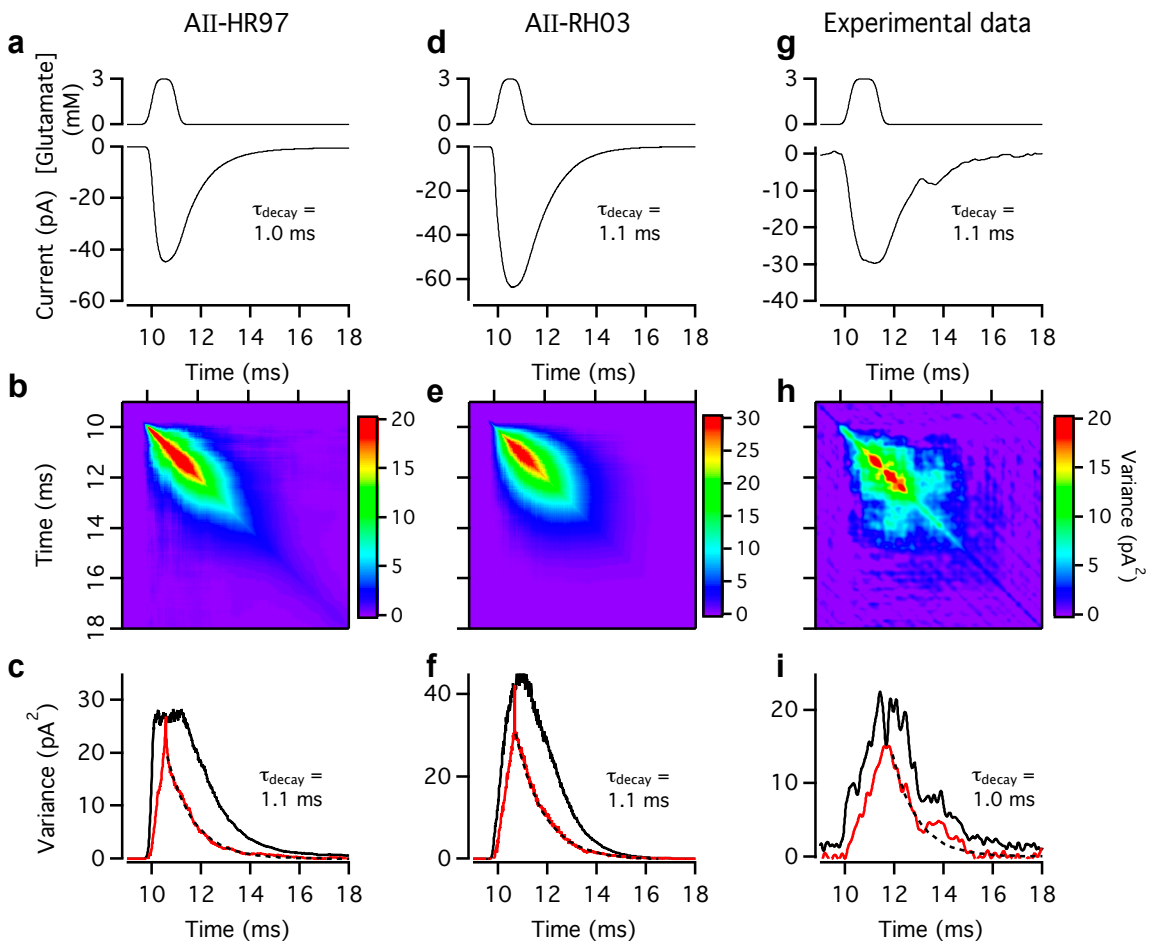

Fig. 9 (Hartveit et al., 2017)

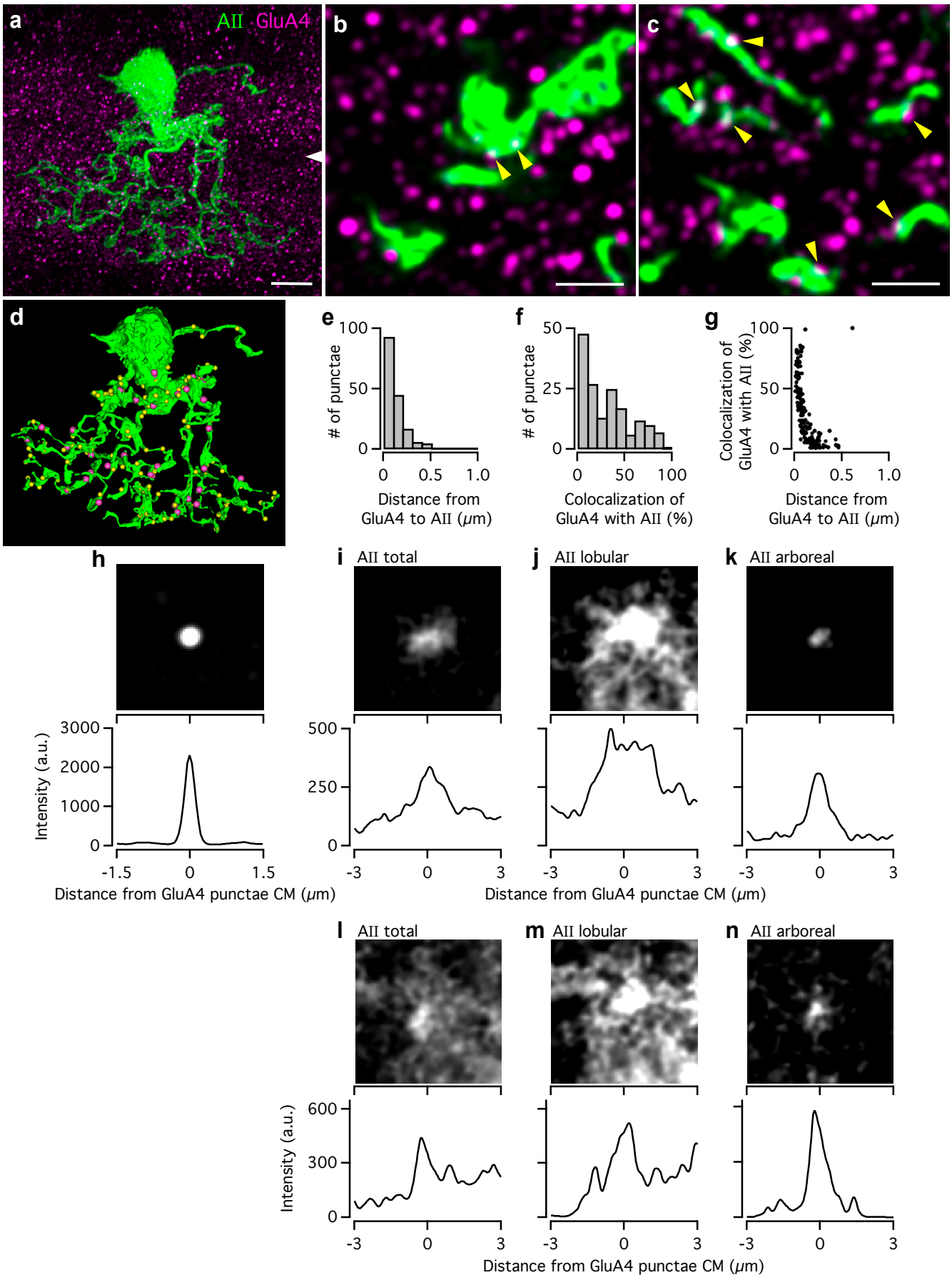

Fig. 10 (Hartveit et al., 2017)

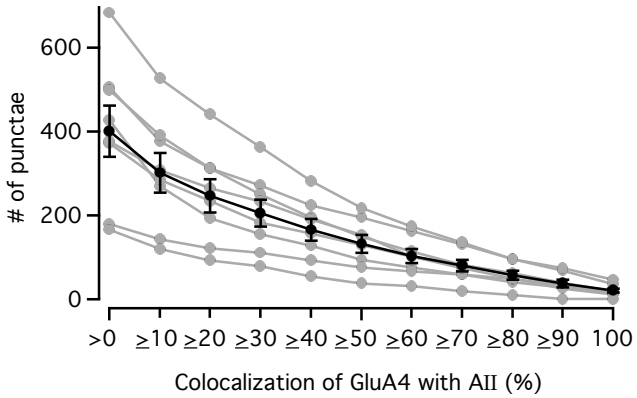

Figure 11 (Hartveit et al., 2017)

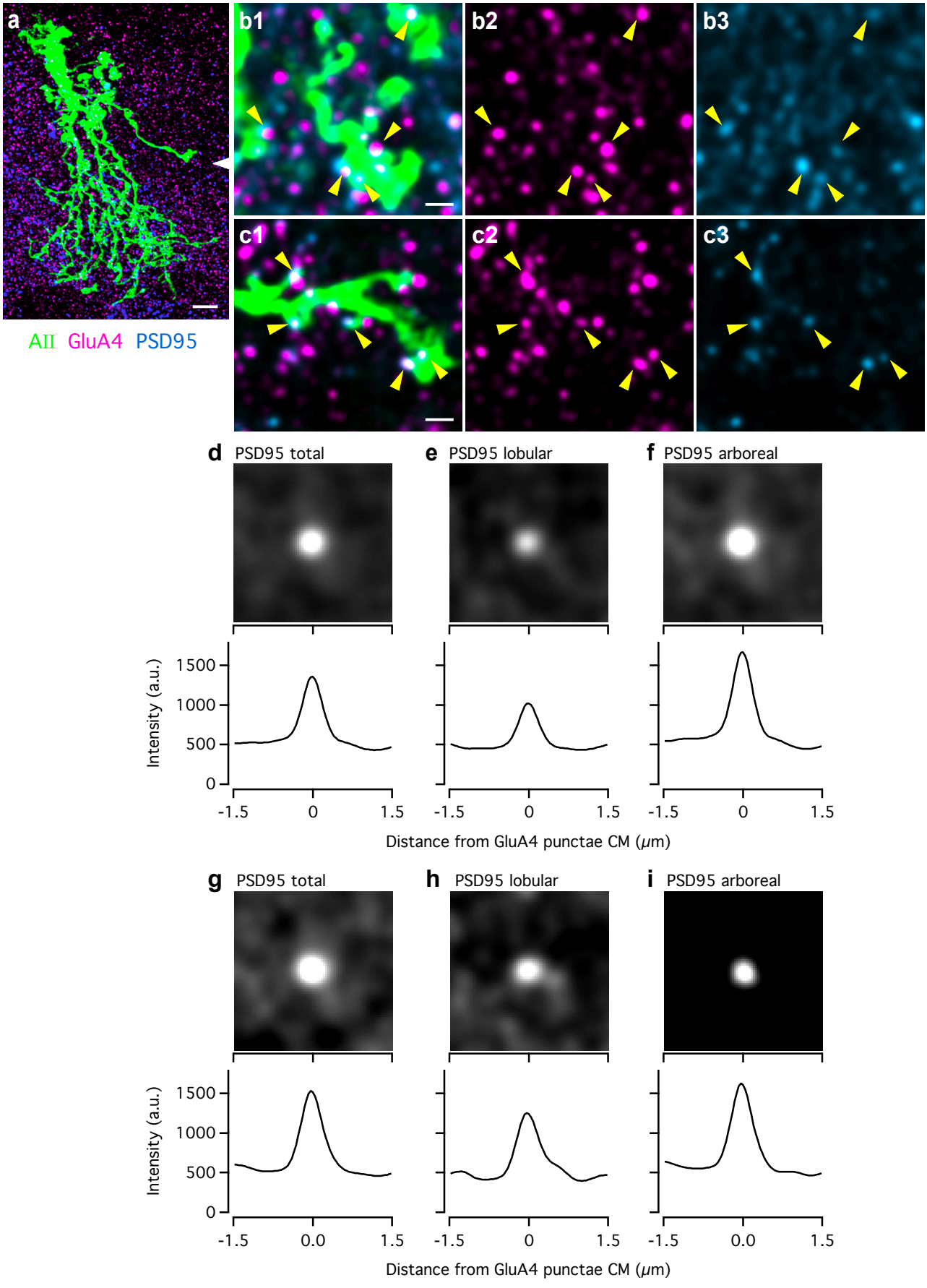

Fig. 12 (Hartveit et al., 2017)

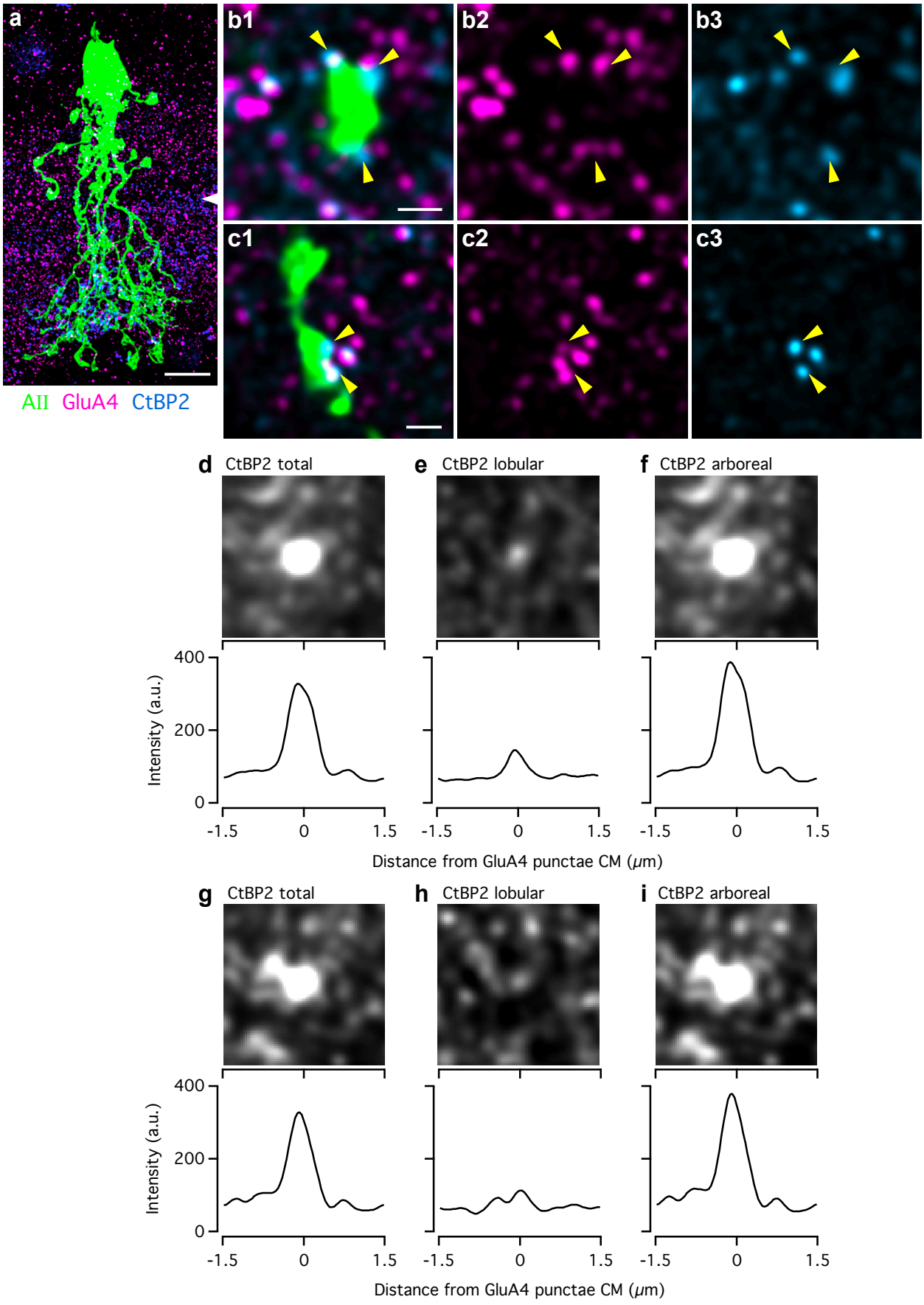

Fig. 13 (Hartveit et al., 2017)